Theor. Comput. Fluid Dyn. (2021) 35:831–873
https://doi.org/10.1007/s00162-021-00591-x

ORIGINAL ARTICLE

Tom Dörffel · Ariane Papke · Rupert Klein · Natalia Ernst · Piotr K. Smolarkiewicz

Dynamics of tilted atmospheric vortices under asymmetric diabatic heating

Received: 20 October 2020 / Accepted: 24 August 2021 / Published online: 10 November 2021

Abstract Päschke et al. (J Fluid Mech, 2012) studied the nonlinear dynamics of strongly tilted vortices subject to asymmetric diabatic heating by asymptotic methods. They found, *inter alia*, that an azimuthal Fourier mode 1 heating pattern can intensify or attenuate such a vortex depending on the relative orientation of the tilt and the heating asymmetries. The theory originally addressed the gradient wind regime which, asymptotically speaking, corresponds to vortex Rossby numbers of order unity in the limit. Formally, this restricts the applicability of the theory to rather weak vortices. It is shown below that said theory is, in contrast, uniformly valid for vanishing Coriolis parameter and thus applicable to vortices up to low hurricane strengths. An extended discussion of the asymptotics as regards their physical interpretation and their implications for the overall vortex dynamics is also provided in this context. The paper's second contribution is a series of three-dimensional numerical simulations examining the effect of different orientations of dipolar diabatic heating on idealized tropical cyclones. Comparisons with numerical solutions of the asymptotic equations yield evidence that supports the original theoretical predictions of Päschke et al. In addition, the influence of asymmetric diabatic heating on the time evolution of the vortex centerline is further analyzed, and a steering mechanism that depends on the orientation of the heating dipole is revealed. Finally, the steering mechanism is traced back to the correlation of dipolar perturbations of potential temperature, induced by the vortex tilt, and vertical velocity, for which diabatic heating not necessarily needs to be responsible, but which may have other origins.

Keywords Hurricanes · Tropical cyclones · Asymptotic analysis · Idealized simulations

1 Introduction

Atmospheric vortex intensification and attenuation, and the associated evolution of vortex structure remain a topic of intense investigations. As Smith and Montgomery [20] point out in their review article, intricate interactions of boundary layer processes, moist thermodynamics, multiscale stochastic deep convection, and the vortex-scale fluid dynamics produce the observed, sometimes extremely rapid intensification of incipient hurricanes. They also emphasize that, despite the deep insights that have been gained in many studies of

Communicated by William Dewar.

T. Dörffel · A. Papke · R. Klein (✉)
FB für Mathematik und Informatik, Freie Universität Berlin, Berlin, Germany
E-mail: rupert.klein@fu-berlin.de

N. Ernst
Zuse Institute Berlin, Berlin, Germany

P. K. Smolarkiewicz
National Center for Atmospheric Research, Boulder, CO 80307, USA

idealized axisymmetric flow models [6,18,19,37], asymmetries of vortex structure, convection patterns, and boundary layer structure have been observed to be important for vortex intensification in real-life situations, see, e.g., recent work by Callaghan [2], Rios-Berrios [34] and references therein.

This study focuses on the principal response mechanisms of *Tropical cyclone*-like (TC) atmospheric vortices to asymmetric diabatic heating following the theory of Päschke et al. [26]. Thus, neglecting boundary layer effects, we analyze both the structure and intensity of a tilted vortex under the influence of different configurations of explicitly prescribed asymmetric heating. In doing so, we adopt the point of view of, among others, Nolan and Montgomery [23], Nolan and Grasso [22], Nolan et al. [24] that latent heat release from condensation can be modeled, with limitations, by external diabatic heat sources in dry air. In the cited studies, non-axisymmetric heating patterns were shown to have at most a small effect on vortex strength within the framework of linearizations about an axisymmetric upright vortex. These results of linear theory were corroborated in Nolan and Grasso [22], Nolan et al. [24] by comparison with fully nonlinear three-dimensional simulations. In contrast, by both analytical and numerical examination, we demonstrate that the particular flow structure of a strongly tilted slender vortex, i.e., a vortex whose vorticity is confined to a narrow peak near the vortex center, does allow for leading-order effects on vortex strength that are associated with asymmetric heating alone and that cannot be captured by linearized analyses.

In concentrating on the effects of purely asymmetric heating, we do not include any axisymmetric components of the heating pattern on purpose. As a consequence, the tests of the theory in this paper do not include secondary circulations (see explanation following Eq. (1) below). This also excludes phenomena such as the formation of an eye wall or of an anticyclonic upper level outflow which we hope to address in future studies. Investigating incipient hurricanes that develop in the tropical Atlantic, Marks et al. [17], Marks [16], and Dunkerton et al. [5] revealed, that such vortices can exhibit very strong tilt. Thus, for instance, the locations of the vortex center at heights equivalent to the 925 and 200 hPa pressure levels are located about 200 km apart, e.g., in ([16], figure 18) and ([5], figure 21). This amounts to an overall vortex tilt at a scale comparable to the vortex diameter, i.e., to a situation that without further assumptions does not allow for linearizations about an upright vortex. In fact, in characterizing the wind field of Hurricane Norbert (1984), Marks et al. [17] already utilized the concept of a height- and generally also time-dependent vortex center. Specifically, they considered barycenters of vorticity coinciding with a tilted *centerline*. Both, the interaction with a non-stationary environment and local self-induction of the vortex lead to a generally time-dependent vortex centerline. In a series of recent studies Chen and Gopalakrishnan [3] and Leighton et al. [13] examined the response of moist convection and vortex intensity to changes in the environmental large scale flow by means of high-resolution idealized and non-idealized simulations. They found evidence of interactions between the asymmetric and tilted vortex core structure and the environment. The incorporation of such non-stationary strong tilts, described explicitly by a time dependent centerline, in a theory for vortex evolution is one of the key structural aspects in the analysis of Päschke et al. [26], which we revisit in the present work. Here we would also like to point to Davies et al. [4], who already provide evidence that asymmetric diabatic heating can directly influence vortex tilt.

Päschke et al. [26] analyzed the dynamics of such strongly tilted atmospheric vortices in the gradient wind regime by matched asymptotic expansions. They obtained a closed and coupled set of evolution equations for the primary circulation structure and the vortex centerline. Their theory describes, in effect, a nonlinear large-tilt variant of the precessing quasi-modes studied earlier in the context of small perturbations of an upright vortex by Reasor and Montgomery [30] (see also, e.g., [31], and references therein). Within their asymptotic framework, Päschke et al. [26] demonstrated that, in a strongly tilted vortex, purely asymmetric heating patterns with zero azimuthal mean can have a comparable impact on vortex intensity as axisymmetric ones.

As, by its very definition, the gradient wind regime is restricted to vortex Rossby numbers of order unity, this theory has been suspected to be applicable only to rather weak vortices with intensities relatively far from the interesting regime in which structural transitions from tropical storms to hurricanes may occur. To allow for vortices in this transition regime, we consider here in the first part of the paper the dynamics of mesoscale atmospheric vortices $L_{\mathrm{mes}} \sim 100\,\mathrm{km}$ that extend vertically across the depth of the troposphere $h_{\mathrm{sc}} \sim 10\,\mathrm{km}$ but feature large vortex Rossby number $\mathrm{Ro}_{\mathrm{mes}} \gg 1$. We use the asymptotic techniques introduced by Päschke et al. [26] and recycle many of their technical steps. As indicated in Fig. 1, we assume vortices with nearly axisymmetric core structure at each horizontal level, and we allow for strong vortex tilt such that the vortex centers observed at different heights may be displaced horizontally relative to each other by distances comparable to the vortex core size L_{mes}.

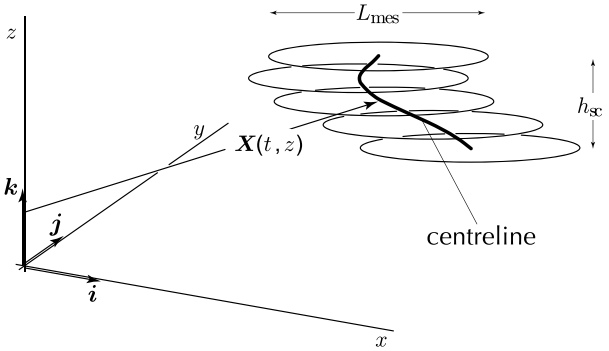

Fig. 1 Sketch of the spacial scaling regime for vortices in this work. In each horizontal plane the vortex is axisymmetric to leading order while the vortex center line position $\boldsymbol{X}(t, z)$ covers horizontal distances comparable to the vortex core size (adapted from Päschke et al. [26]).

One of the main findings of Päschke et al. [26] was the following evolution equation for the primary circulation described by the axisymmetric leading-order circumferential velocity, u_θ, valid for time scales large compared to the vortex turnover time scale,

$$\frac{\partial u_\theta}{\partial t} + w_0 \frac{\partial u_\theta}{\partial z} + u_{r,00}\left(\frac{\partial u_\theta}{\partial r} + \frac{u_\theta}{r} + f_0\right) = -u_{r,*}\left(\frac{u_\theta}{r} + f_0\right) . \tag{1}$$

Here (t, r, z) are the appropriately rescaled time, radial, and vertical coordinates, f_0 is the Coriolis parameter, and w_0 and $u_{r,00}$ are the axisymmetric components of the vertical and radial velocities, i.e., the components of the secondary circulation, that are induced by *the axisymmetric mean heating patterns*. The apparent radial velocity $u_{r,*}$ results from an interaction of the vortex tilt with the asymmetric first circumferential Fourier mode of the vertical velocity. In particular,

$$u_{r,*} = \frac{1}{2\pi}\int_{-\pi}^{\pi} w\, \boldsymbol{e}_r \cdot \frac{\partial \boldsymbol{X}}{\partial z}\, \mathrm{d}\theta\,, \tag{2}$$

where $\boldsymbol{X}(t, z)$ is the time dependent vortex centerline position at height z (see Fig. 1), w is the vertical velocity, and $\boldsymbol{e}_r = \boldsymbol{i}\cos(\theta) + \boldsymbol{j}\sin(\theta)$ is the radial unit vector of a horizontal polar coordinate system attached to the centerline.

$\boldsymbol{X}(t, z)$ itself is governed by the *centerline equation*:

$$\frac{\partial \boldsymbol{X}}{\partial t} = \boldsymbol{u}_s + (\boldsymbol{X}\cdot\nabla)\,\boldsymbol{u}_s + \ln\left(\frac{1}{\delta}\right)\boldsymbol{k}\times\boldsymbol{M}_1 + \boldsymbol{k}\times\boldsymbol{\Psi}\ , \tag{3}$$

where $\boldsymbol{u}_s(t, x, y, z)$ expresses the externally imposed background wind field, δ is the small parameter giving rise to the asymptotic scaling, $\boldsymbol{k}$ the vertical unit vector, $\boldsymbol{M}_1$ is a weighted curvature measure of $\boldsymbol{X}$ and $\boldsymbol{\Psi}$ evaluates Fourier-1 modes of vertical velocity resulting from both, diabatic heating and adiabatic balances within a tilted vortex. In the adiabatic case and without vertical wind shear, equation (3) simplifies to a linear Schrödinger-like equation exhibiting undamped precession of eigenmodes as known from linear and nonlinear perturbation theories and from three-dimensional simulations (see, e.g., [28,30,36,40], and references therein). More details on the expressions for $\boldsymbol{M}_1$ and $\boldsymbol{\Psi}$ follow in the further course of this article.

Note that for the rest of this paper we neglect the background wind $\boldsymbol{u}_s$, because we are interested in highlighting a particular intrinsic interaction of asymmetric heating patterns (without an axisymmetric component) with the otherwise free dynamics of a tilted vortex.

The neglection of boundary layer effects and of the associated low level inward mass fluxes imply that the present analysis cannot describe the substantial secondary circulations, including those in the hurricane eye, observed in fully developed hurricanes. Therefore, we expect the theory to be applicable to incipient hurricanes and the early onset of a secondary circulation only. Especially for those comparably weak TCs, however, recent observational studies [8,9,36] have shown that phases of strong intensity changes are connected to localized and asymmetrically distributed convective events. To this end, in the present work we restrict to effects of purely asymmetric heating. Investigations of how these effects interact with external shear and a secondary circulation are deferred to forthcoming studies.

To summarize the findings of work that is to follow:

1. The evolution equation for the core structure of a strongly tilted vortex from (1) is uniformly valid as $f_0 \to 0$ so that it holds, in particular, also for $\mathrm{Ro}_{\mathrm{mes}} \gg 1$, i.e., for vortices of moderate hurricane strength. In other words: For $\mathrm{Ro}_{\mathrm{mes}} \geq 1$ the structure of the leading-order equations does not change as $f_0 \to 0$.
2. The mechanism of vortex spin-up (spin-down) by purely asymmetric heating of a tilted vortex is traced back analytically to an effective circumferential mean vertical mass flux divergence that arises when the first Fourier mode diabatic heating and the vortex tilt correlate negatively (positively).
3. Asymmetric heating introduces a forcing of the vortex motion which can accelerate/decelerate the centerline precession and/or increase/decrease its tilt depending on the relative orientation of tilt and heating dipole.
4. Equation (1) can be recast into a balance equation for kinetic energy, $e_{\mathrm{k}} = \rho_0 \frac{u_\theta^2}{2}$,

$$\left(re_{\mathrm{k}}\right)_t + \left(ru_{r,00}\left[e_{\mathrm{k}} + \widetilde{p}\right]\right)_r + \left(rw_0\left[e_{\mathrm{k}} + \widetilde{p}\right]\right)_z = \frac{r\rho_0}{N^2\overline{\Theta}^2}\left(\widetilde{\Theta}\cdot Q_\Theta\right)_0 \tag{4}$$

   in line with the theory by Lorenz [14] for available potential energy (APE) generation and its conversion to mechanical energy. Here $\widetilde{p}$ is the relevant pressure perturbation, $\widetilde{\Theta}$, Q_Θ are the potential temperature perturbations and the diabatic heating, respectively, and $(\cdot)_0$ corresponds to the axisymmetric mean. In (4), it encodes the correlation of potential temperature perturbation and diabatic heating. N and $\overline{\Theta}$ are the Brunt–Väisälä frequency and the background potential temperature stratification, respectively. Equation (4) states that, except for a conservative redistribution of kinetic energy due to advection and the work of the pressure perturbation, $\tilde{p}$, positive correlations of diabatic sources and potential temperature perturbations generate the potential energy available for increasing the kinetic energy of the vortex.
   Nolan et al. [24] study the effects of asymmetric diabatic heating on vortex strength in a linearized model. One of their conclusions is that "... purely asymmetric heating generally leads to vortex weakening, usually in terms of the symmetric energy, and always in terms of the low-level wind." The present theory shows that this conclusion does not hold up in case of a strongly tilted vortex, but that in this case symmetric and suitably arranged asymmetric heating have vortex intensification/attenuation efficiencies of the same order of magnitude.
5. The intensification (attenuation) mechanism due to asymmetric diabatic heating is traced back to geometrical properties of the vertical velocity, more precisely that part which positively (negatively) correlates with the potential temperature perturbation caused by the structure of the tilted vortex. Diabatic heating, in fact, turns out to cause those vertical motions at leading order following the weak temperature gradient approximation in the present setting. However, there is no need for diabatic heating in general as vortex-scale averaged vertical motions can be (and most likely will be) caused by different driving forces, such as multiscale convection.
6. The theory compares favorably with three-dimensional numerical simulations based on the compressible Euler equations.

To arrive at these results, we first recount the governing equations and the principles of our analytical approach in Sect. 2, and then revisit the derivations by Päschke et al. [26]. A discussion of the scaling regime is given in Sect. 3 to investigate the influence of the Coriolis effect (item (1)). The asymptotic vortex core expansion is carried out in Sect. 4, and this analysis gives rise to a physical interpretation of the intensification/attenuation by asymmetric heating referred to in item (2). In Sect. 5 we establish the kinetic energy balance of item (4). Section 6 presents results of the theory in comparison with three-dimensional computational simulations to corroborate items (3), (5), and (6). Section 7 provides conclusions and an outlook.

2 Dimensionless governing equations and distinguished limits

2.1 Governing equations

The dimensionless inviscid rotating compressible flow equations for an ideal gas with constant specific heat capacities in the beta plane approximation form the basis for the subsequent asymptotic analysis:

$$\frac{\partial \boldsymbol{u}}{\partial t} + \boldsymbol{u}\cdot\nabla_{\!\shortparallel}\boldsymbol{u} + w\frac{\partial \boldsymbol{u}}{\partial z} + \frac{1}{\mathrm{M}^2}\frac{1}{\rho}\nabla_{\!\shortparallel}p + \frac{1}{\mathrm{Ro}}\left(1+\widehat{\beta}y\right)\boldsymbol{k}\times\boldsymbol{u} = 0\,, \tag{5a}$$

Table 1 Characteristic atmospheric flow parameters

Gravitational acceleration	$g = 9.81\ \mathrm{m\,s^{-2}}$
Coriolis parameter ($\phi = 30°\,\mathrm{N}$)	$f_{\mathrm{ref}} = 7.3 \times 10^{-5}\ \mathrm{s^{-1}}$
$(\mathrm{d}f/\mathrm{d}y)_0$ ($\phi = 30°\,\mathrm{N}$)	$\beta_{\mathrm{ref}} = 2.0 \times 10^{-11}\ \mathrm{m^{-1}\,s^{-1}}$
Pressure	$p_{\mathrm{ref}} = 10^5\ \mathrm{Pa}$
Temperature	$T_{\mathrm{ref}} = 300\ \mathrm{K}$
Brunt–Väisälä frequency	$N_{\mathrm{ref}} = 10^{-2}\ \mathrm{s^{-1}}$
Dry air gas constant	$R = 287\ \mathrm{m^2\,s^{-2}\,K^{-1}}$
Isentropic exponent	$\gamma = 1.4$

Table 2 Derived reference values for nondimensionalization

Density	$\rho_{\mathrm{ref}} = \dfrac{p_{\mathrm{ref}}}{RT_{\mathrm{ref}}}$	$\sim$	$1.16\ \mathrm{kg\,m^{-3}}$
Potential temperature	$\Delta\Theta = T_{\mathrm{ref}} \dfrac{h_{\mathrm{sc}} N_{\mathrm{ref}}^2}{g}$	$\sim$	$40\ \mathrm{K}$
Velocity	$u_{\mathrm{ref}} = \dfrac{\tan\phi}{\pi/2} \dfrac{N_{\mathrm{ref}}^2}{f_{\mathrm{ref}}^2} \beta h_{\mathrm{sc}}^2$	$\sim$	$10\ \mathrm{m\,s^{-1}}$
Length	$h_{\mathrm{sc}} = \dfrac{p_{\mathrm{ref}}}{g\rho_{\mathrm{ref}}}$	$\sim$	$8.8\ \mathrm{km}$
Time	$t_{\mathrm{ref}} = \dfrac{h_{\mathrm{sc}}}{u_{\mathrm{ref}}}$	$\sim$	$10^3\ \mathrm{s}$

$$\frac{\partial w}{\partial t} + \boldsymbol{u}\cdot\nabla_{\shortparallel} w + w\frac{\partial w}{\partial z} + \frac{1}{\mathrm{M}^2}\frac{1}{\rho}\frac{\partial p}{\partial z} = -\frac{1}{\mathrm{Fr}^2}, \tag{5b}$$

$$\frac{\partial \rho}{\partial t} + \boldsymbol{u}\cdot\nabla_{\shortparallel}\rho + w\frac{\partial \rho}{\partial z} + \rho\nabla_{\shortparallel}\cdot\boldsymbol{u} + \rho\frac{\partial w}{\partial z} = 0, \tag{5c}$$

$$\frac{\partial \Theta}{\partial t} + \boldsymbol{u}\cdot\nabla_{\shortparallel}\Theta + w\frac{\partial \Theta}{\partial z} = Q_\Theta, \tag{5d}$$

$$\rho\Theta = p^{\frac{1}{\gamma}} \tag{5e}$$

Here, p, ρ, Θ, $\boldsymbol{u}$, w are rescaled pressure, density, potential temperature, and the horizontal and vertical velocities. γ is the specific heat ratio.

The three-dimensional gradient is $\nabla = \nabla_{\shortparallel} + \boldsymbol{k}\,\partial/\partial z$ with the horizontal gradient $\nabla_{\shortparallel} = \boldsymbol{i}\,\partial/\partial x + \boldsymbol{j}\,\partial/\partial y$, the zonal, meridional, and vertical coordinates (x, y, z), and the related unit vectors $(\boldsymbol{i}, \boldsymbol{j}, \boldsymbol{k})$. Finally, t is the time variable and Q_Θ is a diabatic source term.

Table 1 lists general characteristics of the near-tropical atmosphere. Together with the combined values in Table 2 they form reference values for nondimensionalization. Let an asterisk denote dimensional quantities, then the unknowns and coordinates in (5) are

$$p = \frac{p^*}{p_{\mathrm{ref}}}, \quad \rho = \frac{\rho^*}{\rho_{\mathrm{ref}}}, \quad (\boldsymbol{u}, w) = \frac{(\boldsymbol{u}^*, w^*)}{u_{\mathrm{ref}}}, \quad (\boldsymbol{x}, z) = \frac{(\boldsymbol{x}^*, z^*)}{h_{\mathrm{sc}}}, \quad t = \frac{t^* u_{\mathrm{ref}}}{h_{\mathrm{sc}}}. \tag{6}$$

Note that $u_{\mathrm{ref}}/h_{\mathrm{sc}}$ is an estimate of the large-scale thermal wind shear, and $\boldsymbol{x} = \boldsymbol{i}x + \boldsymbol{j}y$ is the horizontal coordinate vector.

In deriving the dimensionless equations (5) using the quantities from Tables 1 and 2 the Mach, internal wave Froude, and Rossby numbers, and the β-parameter

$$\begin{aligned} \mathrm{M} &= \frac{u_{\mathrm{ref}}}{\sqrt{RT_{\mathrm{ref}}}} \approx 3.4\cdot 10^{-2} & \mathrm{Ro} &= \frac{u_{\mathrm{ref}}}{f_{\mathrm{ref}} h_{\mathrm{sc}}} \approx 13.3 \\ \mathrm{Fr} &= \frac{u_{\mathrm{ref}}}{N_{\mathrm{ref}} h_{\mathrm{sc}}} \approx 1.1\cdot 10^{-1} & \widehat{\beta} &= \frac{\beta_{\mathrm{ref}} h_{\mathrm{sc}}}{f_{\mathrm{ref}}} \approx 2.7\cdot 10^{-3} \end{aligned}, \tag{7}$$

emerge naturally. These are replaced with functions of a single small expansion parameter $\varepsilon \ll 1$ through the distinguished limits

$$\mathrm{M} = \varepsilon^{3/2}\,, \quad \mathrm{Fr} = \frac{\varepsilon}{N}\,, \quad \mathrm{Ro} = \frac{1}{\varepsilon f}\,, \quad \widehat{\beta} = \varepsilon^3 \beta\,, \tag{8}$$

in line with the multiscale asymptotic modeling framework of Klein [11]. Here $(N, f, \beta) = \mathcal{O}(1)$ as $\varepsilon \to 0$, with concrete values

$$N = 0.91\,, \quad f = 0.75\,, \quad \beta = 2.7 \tag{9}$$

derived from (7) for $\varepsilon = \mathrm{M}^{2/3} = 0.105$. Replacing the characteristic numbers according to (8) we obtain

$$\frac{\partial \boldsymbol{u}}{\partial t} + \boldsymbol{u} \cdot \nabla_{\!\shortparallel} \boldsymbol{u} + w \frac{\partial \boldsymbol{u}}{\partial z} + \frac{1}{\varepsilon^3} \frac{1}{\rho} \nabla_{\!\shortparallel} p + \varepsilon \left(f + \varepsilon^3 \beta y \right) \boldsymbol{k} \times \boldsymbol{u} = 0, \tag{10a}$$

$$\frac{\partial w}{\partial t} + \boldsymbol{u} \cdot \nabla_{\!\shortparallel} w + w \frac{\partial w}{\partial z} + \frac{1}{\varepsilon^3} \frac{1}{\rho} \frac{\partial p}{\partial z} = -\frac{1}{\varepsilon^3}, \tag{10b}$$

$$\frac{\partial \rho}{\partial t} + \boldsymbol{u} \cdot \nabla_{\!\shortparallel} \rho + w \frac{\partial \rho}{\partial z} + \rho \nabla_{\!\shortparallel} \cdot \boldsymbol{u} + \rho \frac{\partial w}{\partial z} = 0, \tag{10c}$$

$$\frac{\partial \Theta}{\partial t} + \boldsymbol{u} \cdot \nabla_{\!\shortparallel} \Theta + w \frac{\partial \Theta}{\partial z} = Q_\Theta, \tag{10d}$$

$$\rho \Theta = p^{\frac{1}{\gamma}}. \tag{10e}$$

whereas f and β appear explicitly in (10), N characterizes the background stratification of potential temperature and will be invoked below where we define the initial conditions for the vortex flow.

Equations (10) will form the basis for the subsequent asymptotic analysis for $\varepsilon \ll 1$, although, following [26], much of the expansions will proceed in terms of the small parameter

$$\delta = \sqrt{\varepsilon}\,. \tag{11}$$

3 Scaling regime for large vortex Rossby number and strong tilt

Here we set up the asymptotic scalings for our analysis in terms of typical orders of magnitude of several characteristics of tropical storms and hurricanes.

3.1 Vortex core size, intensity, and evolution time scale

Vortex core sizes, independent of what are the specific definitions used, are found in the range of 50 km to 200 km, while wind speeds in the transition regime from storms to hurricanes are around 30 m/s [7]. With $\delta^2 \equiv \varepsilon \sim 1/10$, $h_{\mathrm{sc}} \sim 10\,\mathrm{km}$, and $u_{\mathrm{ref}} \sim 10\,\mathrm{m/s}$, these data correspond well with

$$L_{\mathrm{v}} \sim h_{\mathrm{sc}}/\delta^2 \approx 100\,\mathrm{km}\,, \quad u_{\max} \sim u_{\mathrm{ref}}/\delta \approx 33\,\mathrm{m/s}\,, \quad \delta p_{\mathrm{v}} \sim \delta^4 p_{\mathrm{ref}}\,, \tag{12}$$

for a characteristic vortex core size L_{v}, a typical wind speed, and the associated depression in the vortex core, respectively. Note that the vortex core size itself is of subordinate interest since the effective Rossby number determines the scaling regime. Further, note that these scalings deviate from those adopted by Päschke et al. [26], who considered systematically larger radii of the order $L_{\mathrm{v}} \sim h_{\mathrm{sc}}/\delta^3$ needed for direct matching to a quasi-geostrophic large scale outer flow. From their work we recall, however, that the vortex core structure and tilt develop on a time scale t_{v} that is by $1/\delta^2$ longer than the vortex core turnover time scale $t_{\mathrm{to}} = L_{\mathrm{v}}/u_{\max}$. Thus, in view of (12), we will follow the vortex core evolution on the time scale

$$t_{\mathrm{v}} = \frac{t_{\mathrm{to}}}{\delta^2} = \frac{1}{\delta^2} \frac{h_{\mathrm{sc}}}{\delta^2} \frac{\delta}{u_{\mathrm{ref}}} = \frac{t_{\mathrm{ref}}}{\delta^3} \sim 10\,\mathrm{h}. \tag{13}$$

The scalings in (12) and (13) include the regime of "rapid intensification," defined by NOAA's National Hurricane Center[1] to denote maximum wind accelerations of 30 kt ($\sim$ 15 m/s) in 24 h.

Also, the adopted scalings describe a vortex in the cyclostrophic regime since

$$\frac{u_\theta^2}{r} = \mathscr{O}\left(\frac{u_{\mathrm{ref}}^2}{h_{\mathrm{sc}}}\right) \qquad \text{whereas} \qquad f_{\mathrm{ref}}\, u_\theta = \mathscr{O}\left(\delta \frac{u_{\mathrm{ref}}^2}{h_{\mathrm{sc}}}\right), \tag{14}$$

i.e., the Coriolis term is subordinate to the centripetal acceleration in the horizontal momentum balance in this regime. Accordingly, the vortex Rossby number is large,

$$\mathrm{Ro_v} = \frac{u_{\max}}{f_0 L_{\mathrm{v}}} = \mathrm{Ro}\frac{u_{\max}}{u_{\mathrm{ref}}}\frac{h_{\mathrm{sc}}}{L_{\mathrm{v}}} = \mathscr{O}\left(\delta^{-2-1+2}\right) = \mathscr{O}\left(\frac{1}{\delta}\right). \tag{15}$$

3.2 Co-moving coordinates for a strongly tilted vortex

Following Päschke et al. [26], we resolve the flow dynamics on the vortex precession and core evolution time scale t_{v} from (13). The appropriate time coordinate is

$$\widehat{t} = \delta^3 t\,. \tag{16}$$

For the core structure analysis we introduce vortex centered horizontal coordinates

$$\boldsymbol{x} = \frac{1}{\delta^2}\left(\boldsymbol{X}(\widehat{t}, z) + \widehat{\boldsymbol{x}}\right) \tag{17}$$

where $\boldsymbol{X}(\widehat{t}, z)$ is the horizontal position of the vortex centerline at height z and $\widehat{\boldsymbol{x}}$ is the relative horizontal offset. With this scaling $\widehat{\boldsymbol{x}}$ resolves the core scale L_{v} from (12) and the centerline covers comparable distances. This justifies the notion of "strong tilt."

In the sequel we use polar coordinates in horizontal planes, i.e.,

$$\widehat{\boldsymbol{x}} = \widehat{x}\,\boldsymbol{i} + \widehat{y}\,\boldsymbol{j} \qquad \text{where} \qquad \begin{cases} \widehat{x} = \widehat{r}\cos\theta\,; & \boldsymbol{i} = \boldsymbol{e}_r\cos\theta - \boldsymbol{e}_\theta\sin\theta \\ \widehat{y} = \widehat{r}\sin\theta\,; & \boldsymbol{j} = \boldsymbol{e}_r\sin\theta + \boldsymbol{e}_\theta\cos\theta \end{cases} \tag{18}$$

with $\boldsymbol{e}_r$ and $\boldsymbol{e}_\theta$ the radial and circumferential unit vectors, respectively. The transformation rules for derivatives in these coordinates read

$$\nabla_{\!\mathrm{h}} = \delta^2\left(\boldsymbol{e}_r\frac{\partial}{\partial\widehat{r}} + \boldsymbol{e}_\theta\frac{1}{\widehat{r}}\frac{\partial}{\partial\theta}\right) \equiv \delta^2\,\widehat{\boldsymbol{\nabla}}\,, \tag{19a}$$

$$\left.\frac{\partial}{\partial z}\right|_{t,x,y} = \left.\frac{\partial}{\partial z}\right|_{\widehat{t},\widehat{r},\theta} - \frac{\partial\boldsymbol{X}}{\partial z}\cdot\widehat{\boldsymbol{\nabla}}\,, \tag{19b}$$

$$\left.\frac{\partial}{\partial t}\right|_{x,y,z} = \delta^3\left(\left.\frac{\partial}{\partial\widehat{t}}\right|_{\mathrm{eso},\theta,\mathrm{z}} - \frac{\partial\boldsymbol{X}}{\partial\widehat{t}}\cdot\widehat{\boldsymbol{\nabla}}\right). \tag{19c}$$

The horizontal velocity is decomposed into the vortex' motion plus the relative velocity,

$$\boldsymbol{u} = \delta\frac{\partial\boldsymbol{X}}{\partial\widehat{t}} + (u_r\,\boldsymbol{e}_r + u_\theta\,\boldsymbol{e}_\theta)\,. \tag{20}$$

For later reference, here are the centerline, represented in the $(\boldsymbol{e}_r, \boldsymbol{e}_\theta)$ basis,

$$\boldsymbol{X} = (X\cos\theta + Y\sin\theta)\;\boldsymbol{e}_r + (-X\sin\theta + Y\cos\theta)\;\boldsymbol{e}_\theta\,, \tag{21}$$

and the Fourier expansion of functions of the circumferential angle, θ,

$$F(\theta) = F_0 + \sum_n \left(F_{n1}\cos(n\theta) + F_{n2}\sin(n\theta)\right)\,. \tag{22}$$

Note that we have exchanged the roles of F_{n1} and F_{n2} relative to their use in [26] as this will streamline the notation throughout the analysis of the orientation of a dipolar field characterized by $\boldsymbol{F}_1 = (F_{11}, F_{12})^T$ relative to the tilt vector $\partial\boldsymbol{X}/\partial z$ below.

[1] http://www.nhc.noaa.gov/aboutgloss.shtml.

3.3 Vortex core expansion scheme

The circumferential velocity is expanded as

$$u_\theta(t,\boldsymbol{x},z;\varepsilon) = \delta^{-1}u_\theta^{(0)}(t,\widehat{r},z) + u_\theta^{(1)}(t,\widehat{r},z) + \delta u_\theta^{(2)}(t,\widehat{r},\theta,z) + \mathcal{O}(\delta), \tag{23a}$$

$$u_r(t,\boldsymbol{x},z;\varepsilon) = \delta u_r^{(2)}(t,\widehat{r},\theta,z) + \mathcal{O}(\delta)\,. \tag{23b}$$

i.e., non-axisymmetry relative to the centerline is allowed for scaling orders from $\mathcal{O}(\delta u_{\mathrm{ref}})$ upwards. Across the core size length scale, L_{v}, such asymmetries induce horizontal divergences of order $u_r/L_{\mathrm{v}} \sim \delta u_{\mathrm{ref}}/(h_{\mathrm{sc}}/\delta^2) = \delta^3 u_{\mathrm{ref}}/h_{\mathrm{sc}}$, see (12). Since the flow field is anelastic to leading order as derived below, this implies the vertical velocity scaling,

$$w(t,\boldsymbol{x},z;\varepsilon) = \delta^3 w^{(0)}(t,\widehat{r},\theta,z) + \mathcal{O}(\delta^3)\,. \tag{24}$$

Expansions for the thermodynamic variables are anticipated as follows,

$$p = p_0 + \delta^2 p_2 \ + \delta^4\left(\widehat{p}^{(4)} \ + \widehat{p}_4\right) + \delta^5\left(\widehat{p}^{(5)} \ + \widehat{p}_5\right) + \mathcal{O}(\delta^5)\,, \tag{25a}$$

$$\rho = \rho_0 + \delta^2\rho_2 \ + \delta^4\left(\widehat{\rho}^{(4)} \ + \widehat{\rho}_4\right) + \delta^5\left(\widehat{\rho}^{(5)} \ + \widehat{\rho}_5\right) + \mathcal{O}(\delta^5)\,, \tag{25b}$$

$$\Theta = \Theta_0 + \delta^2\Theta_2 \ + \delta^4\left(\widehat{\Theta}^{(4)} + \widehat{\Theta}_4\right) + \delta^5\left(\widehat{\Theta}^{(5)} + \widehat{\Theta}_5\right) + \mathcal{O}(\delta^5)\,, \tag{25c}$$

[for plausibility arguments see [26], section 4.1.3]. The variables $p_0(z)$, $p_2(z)$, $\rho_0(z)$, $\rho_2(z)$, and $\Theta_2(z)$ in (25) describe the stationary background (Θ_0 is a constant), $\widehat{p}_i(\widehat{t},z)$, $\widehat{\rho}_i(\widehat{t},z)$, and $\widehat{\Theta}_i(\widehat{t},z)$, are higher-order horizontal means, and the quantities $\widehat{p}^{(i)}(\widehat{t},\widehat{r},\theta,z)$, $\widehat{\rho}^{(i)}(\widehat{t},\widehat{r},\theta,z)$, and $\widehat{\Theta}^{(i)}(\widehat{t},\widehat{r},\theta,z)$ are of prime interest with full spatio-temporal variation.

Note that, owing to the Fourier representation defined in (22), this notational convention "overloads" the subscript $(\cdot)_0$ with a double-meaning, but the distinction should always be clear from the context.

The vortex centerline position is expanded as

$$\boldsymbol{X}(\widehat{t},z) = \boldsymbol{X}^{(0)}(\widehat{t},z) + \mathscr{O}\left(\delta^1\right)\,. \tag{26}$$

4 Asymptotic analysis of the core structure evolution

This section revisits the analysis of Päschke et al. [26] for large vortex Rossby numbers focusing on the evolution equation for the primary circulation.

4.1 Asymptotic equation hierarchy for the vortex core

The governing equations transformed to the co-moving coordinates are provided in Appendix A. Inserting the expansion scheme from the previous section we obtain

$$-\frac{(u_\theta^{(0)})^2}{\widehat{r}} + \frac{1}{\rho_0}\frac{\partial\widehat{p}^{(4)}}{\partial\widehat{r}} = 0, \qquad \frac{\partial\widehat{p}^{(4)}}{\partial\theta} = 0 \tag{27a}$$

$$-\frac{2u_\theta^{(0)}u_\theta^{(1)}}{\widehat{r}} + \frac{1}{\rho_0}\frac{\partial\widehat{p}^{(5)}}{\partial\widehat{r}} - f_0 u_\theta^{(0)} = 0, \qquad \frac{\partial\widehat{p}^{(5)}}{\partial\theta} = 0 \tag{27b}$$

from the horizontal momentum balance at leading and first order, respectively. Each line in (27) displays the respective radial balance first and the circumferential balance as the second equation. We observe from the radial component in (27a) that the vortex is in cyclostrophic balance to leading order which implies large vortex Rossby number. The Coriolis effect enters only as a first-order perturbation in the present regime as seen in the radial component of (27b). The pressure perturbations $p^{(4)}$, $p^{(5)}$ inherit the assumed axisymmetry of $u_\theta^{(0)}$, $u_\theta^{(1)}$ thanks to the leading and first-order circumferential momentum balances in (27a) and (27b), respectively.

The full second-order horizontal momentum equations are listed in Appendix B, equations (69), but for the rest of the paper we only need the circumferential average of the circumferential component (69b). Letting

$\psi_0 \equiv \frac{1}{2\pi}\int_{-\pi}^{\pi}\psi(\theta)\,\mathrm{d}\theta$ denote the circumferential average of some θ-dependent variable ψ in line with (22), we have

$$\frac{\partial u_\theta^{(0)}}{\partial t} + w_0^{(0)}\frac{\partial u_\theta^{(0)}}{\partial z} + u_{r,0}^{(2)}\left(\frac{\partial u_\theta^{(0)}}{\partial \widehat{r}} + \frac{u_\theta^{(0)}}{\widehat{r}}\right) - u_{r,*}^{(2)}\frac{\partial u_\theta^{(0)}}{\partial \widehat{r}} = 0\,, \tag{28}$$

where

$$u_{r,*}^{(2)} = \left(w^{(0)}\boldsymbol{e}_r \cdot \frac{\partial \boldsymbol{X}^{(0)}}{\partial z}\right)_0 . \tag{29}$$

The flow is hydrostatic up to third-order and in the fourth-order horizontal mean, i.e., we have $\frac{\partial p_i}{\partial z} = -\rho_i$ $(i = 0, 2)$ and $\frac{\partial \widehat{p}_4}{\partial z} = -\widehat{\rho}_4$, whereas

$$\frac{\partial \widehat{p}^{(4)}}{\partial z} - \frac{\partial \boldsymbol{X}^{(0)}}{\partial z}\cdot\boldsymbol{e}_r\frac{\partial \widehat{p}^{(4)}}{\partial \widehat{r}} = -\widehat{\rho}^{(4)}\,. \tag{30}$$

The leading and first-order velocities are horizontal and axisymmetric according to (23), (24) and thus divergence free. The second-order velocity is subject to an anelastic divergence constraint obtained from the mass balance,

$$\frac{\rho_0}{\widehat{r}}\left(\frac{\partial}{\partial \widehat{r}}\left(\widehat{r}u_r^{(2)}\right) + \frac{\partial u_\theta^{(2)}}{\partial \theta}\right) + \frac{\partial}{\partial z}\left(\rho_0 w^{(0)}\right) - \frac{\partial \boldsymbol{X}^{(0)}}{\partial z}\cdot\hat{\boldsymbol{\nabla}}_{\shortparallel}(\rho_0 w^{(0)}) = 0\,. \tag{31}$$

Similarly, the first non-trivial potential temperature transport equation reads

$$\frac{u_\theta^{(0)}}{\widehat{r}}\frac{\partial \widehat{\Theta}^{(4)}}{\partial \theta} + w^{(0)}\frac{\mathrm{d}\Theta_2}{\mathrm{d}z} = Q_\Theta^{(0)}\,, \tag{32}$$

and the equation of state relates the thermodynamic perturbation variables through

$$\widehat{\rho}^{(4)} = \rho_0\left(\frac{\widehat{p}^{(4)}}{\gamma p_0} - \frac{\widehat{\Theta}^{(4)}}{\Theta_0}\right). \tag{33}$$

4.2 Temporal evolution of the vortex structure

Päschke et al. [26] observed that with the aid of (27) and (29)–(33), and given the vortex tilt, $\partial \boldsymbol{X}^{(0)}/\partial z$, as well as the diabatic source term, $Q_\Theta^{(0)}$, one may interpret (28) as a closed evolution equation for the leading circumferential velocity, $u_\theta^{(0)}$.

To corroborate this, we use the Fourier decomposition, (22), for $w^{(0)}$ and the of the centerline in polar coordinates from (21) to obtain

$$u_{r,*}^{(2)} = \left(w^{(0)}\boldsymbol{e}_r\cdot\frac{\partial \boldsymbol{X}^{(0)}}{\partial z}\right)_0 = \frac{1}{2}\left[w_{11}^{(0)}\frac{\partial X^{(0)}}{\partial z} + w_{12}^{(0)}\frac{\partial Y^{(0)}}{\partial z}\right]. \tag{34}$$

Expressions for $w_0^{(0)}$ and $w_{1k}^{(0)}$ for $k = 1, 2$ follow from the Θ–transport equation in (32),

$$w_0^{(0)}\frac{\mathrm{d}\Theta_2}{\mathrm{d}z} = Q_{\Theta,0}^{(0)}\,, \qquad w_{1k}^{(0)}\frac{\mathrm{d}\Theta_2}{\mathrm{d}z} = Q_{\Theta,1k}^{(0)} - (-1)^k\frac{u_\theta^{(0)}}{\widehat{r}}\widehat{\Theta}_{1[3-k]}^{(4)}\,. \tag{35}$$

Since $\widehat{p}^{(4)}$ is axisymmetric (see 27a), $\widehat{p}_{1k}^{(4)} \equiv 0$ and the equation of state, (33), yields $\widehat{\Theta}_{1k}^{(4)}/\Theta_0 = -\widehat{\rho}_{1k}^{(4)}/\rho_0$. With this information, the vertical momentum balance (30) yield

$$\frac{\widehat{\Theta}_{11}^{(4)}}{\Theta_0} = -\frac{\widehat{\rho}_{11}^{(4)}}{\rho_0} = -\frac{1}{\rho_0}\frac{\partial X^{(0)}}{\partial z}\frac{\partial \widehat{p}^{(4)}}{\partial \widehat{r}}\,, \qquad \frac{\widehat{\Theta}_{12}^{(4)}}{\Theta_0} = -\frac{\widehat{\rho}_{12}^{(4)}}{\rho_0} = -\frac{1}{\rho_0}\frac{\partial Y^{(0)}}{\partial z}\frac{\partial \widehat{p}^{(4)}}{\partial \widehat{r}}\,. \tag{36}$$

Using the cyclostrophic balance in (27a) to eliminate $\partial\widehat{p}^{(4)}/\partial\widehat{r}$, and going back to (35) we obtain expressions for the $w_{1k}^{(0)}$ in terms of $u_\theta^{(0)}$, $\partial \boldsymbol{X}^{(0)}/\partial z$, and $Q_\Theta^{(0)}$,

$$w_{1k}^{(0)}\frac{\mathrm{d}\Theta_2}{\mathrm{d}z} = Q_{\Theta,1k}^{(0)} - (-1)^k\Theta_0\frac{\partial X_{[3-k]}^{(0)}}{\partial z}\frac{(u_\theta^{(0)})^3}{\widehat{r}^2} \qquad \Big(k=1,2\Big), \tag{37}$$

where $X_1^{(0)} \equiv X^{(0)}$ and $X_2^{(0)} \equiv Y^{(0)}$. Upon insertion of this result in (34), the second term on the right cancels, so that

$$u_{r,*}^{(2)} = \frac{1}{2\,\mathrm{d}\Theta_2/\mathrm{d}z}\left[Q_{\Theta,11}^{(0)}\frac{\partial X^{(0)}}{\partial z} + Q_{\Theta,12}^{(0)}\frac{\partial Y^{(0)}}{\partial z}\right] \equiv \frac{1}{2\,\mathrm{d}\Theta_2/\mathrm{d}z}\boldsymbol{Q}_{\Theta,1}^{(0)}\cdot\frac{\partial \boldsymbol{X}^{(0)}}{\partial z}. \tag{38}$$

Here we have interpreted the cosine and sine Fourier-1 components of $Q_\Theta^{(0)}$ as the components of a heating dipole vector, $\boldsymbol{Q}_\Theta$, in the horizontal plane.

To find a corresponding expression for $u_{r,0}^{(2)}$ (see the third term in (28)), consider the circumferential average of mass continuity, (31). A brief calculation yields

$$\frac{\partial\left(\widehat{r}\rho_0 u_{r,0}^{(2)}\right)}{\partial\widehat{r}} + \frac{\partial\left(\widehat{r}\rho_0 w_0^{(0)}\right)}{\partial z} - \frac{1}{2}\left[\frac{\partial X^{(0)}}{\partial z}\frac{\partial(\widehat{r}\rho_0 w_{11}^{(0)})}{\partial\widehat{r}} + \frac{\partial Y^{(0)}}{\partial z}\frac{\partial(\widehat{r}\rho_0 w_{12}^{(0)})}{\partial\widehat{r}}\right] = 0 \tag{39}$$

or, equivalently,

$$\frac{\partial\left(\widehat{r}\rho_0\left[u_{r,0}^{(2)} - u_{r,*}^{(2)}\right]\right)}{\partial\widehat{r}} + \frac{\partial\left(\widehat{r}\rho_0\, w_0^{(0)}\right)}{\partial z} = 0 \tag{40}$$

with $u_{r,*}^{(2)}$ defined in (34). Exploiting (37) in that definition and integrating in $\widehat{r}$ requiring that $u_{r,0}^{(2)}$ be finite at $\widehat{r}=0$ we find

$$u_{r,0}^{(2)} = u_{r,00}^{(2)} + u_{r,*}^{(2)}, \tag{41}$$

where

$$u_{r,00}^{(2)} = -\frac{1}{\widehat{r}}\int_0^{\widehat{r}}\frac{r}{\rho_0}\frac{\partial}{\partial z}\left(\rho_0\frac{Q_{\Theta,0}^{(0)}}{\mathrm{d}\Theta_2/\mathrm{d}z}\right)\mathrm{d}r\,. \tag{42}$$

With (35) (first equation), (38), (41), and (42) we have now indeed expressed $w_0^{(0)}$, $u_{r,0}^{(2)}$, and $u_{r,*}^{(2)}$ in terms of $u_\theta^{(0)}$, $\partial \boldsymbol{X}^{(0)}/\partial z$, and $Q_\Theta^{(0)}$ as announced. In the sequel, we may thus derive from (28) how vortex tilt and diabatic heating affect the evolution of the primary circulation.

Remark (item 1): The results in this section match the corresponding result by Päschke et al. [26] with the Coriolis parameter f_0 set to zero. This corroborates our statement (item 1) in the introduction that the vortex amplification/attenuation mechanism described in their work does not depend on the vortex Rossby number being at most of order unity.

5 Discussion of the asymmetric intensification/attenuation mechanism

5.1 The influence of asymmetric heating on the primary circulation

As elaborated in the previous section (28) describes the evolution of the primary circulation in response to external diabatic heating in the present vortex flow regime. Aiming to separate the influence of heating asymmetries from those of axisymmetric effects, we recall from (41) that the net circumferentially averaged radial velocity is entirely a response to diabatic effects, and that it consists of one part, $u_{r,00}^{(2)}$, which, according

to (42) is induced by axisymmetric heating, and a second part, $u^{(2)}_{r,*}$, which, according to (38), arises from first Fourier mode asymmetric heating patterns. Using this decomposition in (28), we rewrite the equation as

$$\frac{\partial u^{(0)}_\theta}{\partial t} + w^{(0)}_0 \frac{\partial u^{(0)}_\theta}{\partial z} + u^{(2)}_{r,00}\left(\frac{\partial u^{(0)}_\theta}{\partial \widehat{r}} + \frac{u^{(0)}_\theta}{\widehat{r}}\right) = -u^{(2)}_{r,*}\frac{u^{(0)}_\theta}{\widehat{r}}\,, \tag{43}$$

which is the large-Rossby ($f_0 \to 0$) version of Eq. (1) announced in the introduction. In this equation, the left-hand side captures the influence of the axisymmetric dynamics and axisymmetric diabatic heating, whereas the right-hand side covers all effects due to the interaction of asymmetric heating and vortex tilt.

5.2 Mechanics of vortex intensification/attenuation by asymmetric heating of a tilted vortex

In the following section we analyze the leading-order mass balance relations given in (39) and (40). We furthermore argue that $u^{(2)}_{r,*}$, given in (38), plays a crucial role in explaining the spin-up mechanism based on asymmetric diabatic heating. In this context we note that, according to (37), the first-order Fourier modes of the vertical velocity involve a contribution from diabatic heating (first term) and one due to the adiabatic dynamics (second term). It is only the contribution by diabatic heating that has an impact on $u^{(2)}_{r,*}$ as seen in (38).

The situation is sketched for the case of asymmetric heating anti-parallel to the tilt in Fig. 2. From the anelastic constraint in (31), averaged in θ, we observe that a vertical velocity dipole with non-zero projection onto the tilt vector generates an averaged radial motion. From Fig. 2, this effect becomes physically transparent: the net vertical mass flow across the tilted-disc control volume through its radial boundary must be accompanied by a compensating radial motion to satisfy the anelastic constraint. In fact, considering mass continuity in centerline-attached coordinates in (39), we can identify the term in brackets as the axisymmetric mean of the vertical mass flux. Equation (40) reveals that this expression is equal to a horizontal mass flux governed by $u^{(2)}_{r,*}$. We therefore conclude that the net vertical outflow in Fig. 2 is compensated in the present balanced vortex situation by a net horizontal inflow to preserve continuity.

This gives rise to a spin-up mechanism that exploits the vertical (tilted) structure of the vortex to gain angular momentum by moving air parcels from larger radii to the center of the vortex. In contrast, the opposite orientation of diabatic Fourier-1 modes leads to an attenuation of the vortex by transporting angular momentum away from the center. We therefore claim that by this mechanism it is possible to influence the overall strength of an atmospheric vortex as will be demonstrated in Sect. 6.

Remark (item 2): This should support the second claim (item 2) in the introduction regarding the physical interpretation of the vortex spin-up or spin-down mechanism involving interactions of asymmetric diabatic heating with the vortex tilt.

5.3 Energy budget for the externally heated vortex

Here we elaborate on how the asymmetric diabatic heating is transferred to kinetic energy of the primary circulation in a tilted vortex. This will be particularly useful in assessing the derived equations within the framework of Available Potential Energy (APE, [14]).

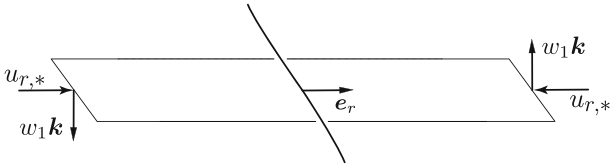

Fig. 2 Vertical cross-section through a slant-cylindrical control volume of a tilted vortex. The curve in the center indicates the position of the centerline, the tilt direction lies in the drawing plane. Net vertical mass transport through the boundary of the control volume, as induced by the vertical velocity dipole $\boldsymbol{w}_1$, is compensated by horizontal mass transport of opposite sign due to mass conservation in the anelastic limit

To this end we multiply (43) by $\rho_0 \widehat{r}\, u_\theta^{(0)}$, use the θ-averaged leading-order mass balance from (40) and recast the advective terms in conservation form to obtain,

$$\frac{\partial}{\partial t}\left(\widehat{r}\rho_0 \frac{u_\theta^2}{2}\right) + \frac{\partial}{\partial \widehat{r}}\left(\widehat{r}\rho_0 u_{r,00}^{(2)} \frac{u_\theta^2}{2}\right) + \frac{\partial}{\partial z}\left(\widehat{r}\rho_0 w_0 \frac{u_\theta^2}{2}\right) = -\widehat{r}\, u_{r,0}^{(2)} \frac{\partial p^{(4)}}{\partial \widehat{r}}\,. \tag{44}$$

Here we have dropped the $^{(0)}$ superscript on $u_\theta^{(0)}$ and $w^{(0)}$ to simplify the notation, and we have used the cyclostrophic radial momentum balance from (27) to introduce the pressure gradient on the right.

This reveals the change of kinetic energy (left-hand side) to result from the work of the pressure force due to the mean radial motion (right-hand side). Some straightforward but lengthy calculations, the details of which are given in Appendix C, yield a direct relation of the kinetic energy balance in (44) to the Lorenz' theory of generation of available potential energy (APE) by diabatic heating,

$$\begin{aligned}(\widehat{r}e_\mathrm{k})_t + \left(\widehat{r}u_{r,00}^{(2)}h_\mathrm{k}\right)_{\hat{r}} + \left(\widehat{r}w_0^{(0)}h_\mathrm{k}\right)_z &= \frac{\widehat{r}\rho_0}{\mathrm{d}\Theta_2/\mathrm{d}z}\frac{1}{\Theta_0}\left[\Theta_0^{(4)}Q_{\Theta,0}^{(0)} + \frac{1}{2}\boldsymbol{\Theta}_1^{(4)}\cdot\boldsymbol{Q}_{\Theta,1}^{(0)}\right] \\ &= \frac{r\rho_0}{N^2\Theta_0^2}\left(\Theta^{(4)}Q_\Theta^{(0)}\right)_0\,,\end{aligned} \tag{45}$$

where $h_\mathrm{k} = e_\mathrm{k} + p^{(4)}$, and $\left(\boldsymbol{\Theta},\, \boldsymbol{Q}_\Theta\right)_1 = (\Theta,\, Q_\Theta)_{11}\,\boldsymbol{i} + (\Theta,\, Q_\Theta)_{12}\,\boldsymbol{j}$ are the dipole vectors spanned by the first circumferential Fourier components of the fourth-order potential temperature perturbation, $\Theta^{(4)}$, and of the diabatic heating function, $Q_\Theta^{(0)}$, respectively.

Equation (45) poses the differential form of the kinetic energy balance. To end up with an integral form as presented in Lorenz [14] we make use of Gauss's theorem which allows us to drop the radial and vertical derivatives assuming $u_{r,00}^{(2)}$ and $w_0^{(2)}$ vanish for sufficiently large $\widehat{r}$ and z, respectively. Conditions under which this constraint for $u_{r,00}^{(2)}$ is satisfied can be derived from (42). The equation shows that we do not only need $Q_{\Theta,0}$ such that the integral converges for large radii, but we need the integral to converge to zero. Thus, when assuming a concentrated pattern of heating with amplitude $\mathscr{O}\left(10^{-4}\,\mathrm{K/s}\right)$ close to the vortex center (in the eyewall) over a surface of $\sim 10^4$ km^2 it would need to be counteracted by contributions with opposite sign, i.e., cooling, but over a much larger surface of $\sim 10^6$ km^2. This simple scale approximation reveals cooling rates of $\mathscr{O}\,(0.1K/d)$ which is by an order of magnitude smaller than observed radiative cooling rates [12,34,35,38], and thus well within reach of the overall radiative balance on larger scales.

For the total (integrated) kinetic energy E_k we find

$$\frac{\mathrm{d}E_k}{\mathrm{d}t} = 2\pi \int_0^\infty \int_0^\infty \frac{\widehat{r}\rho_0}{N^2\Theta_0^2}\left(\Theta^{(4)}Q_\Theta^{(0)}\right)_0 \,\mathrm{d}r\,\mathrm{d}z\,, \tag{46}$$

On the one hand, Lorenz [14] balanced the kinetic energy with the *conversion rate* from APE to kinetic energy (C) and the *dissipation rate* (D) whereas the latter is neglected in our case. In contrast, the analytical expression on the right-hand side of the energy balance equation (46) coincides with the *generation rate* (G) of APE (see Appendix D for details) and not with the *conversion rate*. Therefore, we come to the conclusion that APE is directly converted into kinetic energy and does not accumulate (at leading order). This is the result of the timescale used in the asymptotic analysis as conversion between APE and kinetic energy is accomplished by the advective and pressure-velocity fluxes on faster timescales.

In line with Lorenz [14,15] and as announced in (item 4) of the introduction, this result shows that positive correlations of temperature perturbation and diabatic heating lead to an increase in kinetic energy. The precise form of the right-hand side of (4) as announced in the introduction (item 4) is obtained from (45) by realizing that $(1/\Theta_0)\mathrm{d}\Theta_2/\mathrm{d}z$ is the dimensionless representation of N^2, the square of the Brunt–Väisälä frequency, and that the constant Θ_0 is the leading-order dimensionless background potential temperature $\overline{\Theta} = T_\mathrm{ref}(\Theta_0 + o\,(1))$.

Remark (item 4): Nolan et al. [24], extending prior similar studies, investigate the influence of asymmetric diabatic heating on vortex intensification on the basis of a linearized anelastic model that includes a radially varying base state and baroclinic primary circulation. Their central conclusions are that (1) asymmetric heating patterns quite generally tend to attenuate a vortex, that (2) there are situations in which they can induce amplification, but in these cases their influence is (3) generally rather weak. In fact, they state in their section e:

"... purely asymmetric heating generally leads to vortex weakening, usually in terms of the symmetric energy, and always in terms of the low-level wind." Equation (45) shows, in contrast, that purely asymmetric heating in a tilted vortex can intensify or attenuate a vortex depending on the arrangement of the heating pattern relative to the tilt, and that the efficiencies of symmetric and asymmetric heating in generating kinetic energy are of the same order in the asymptotics as claimed in (item 4) of the introduction.

5.4 Diabatic forcing of the centerline motion

This section highlights aspects of the effects of asymmetric heating on the vortex centerline motion that have not been worked out in detail in our earlier publications. Examinations in Appendix E of the constituents of the centerline equation reveal that the term $\boldsymbol{k} \times \boldsymbol{\Psi}$ splits into an adiabatic and a diabatic contribution due to the linear dependency of $\boldsymbol{\Psi}$ on the vertical velocity dipole $\boldsymbol{w}_1$, where $\boldsymbol{w}_1$ is composed of an adiabatic and a diabatic contribution (see (37)). In particular, the adiabatic expression is of the same analytical form as the diabatic one but evaluated with the adiabatic vertical velocity:

$$\boldsymbol{w}_{1,\mathrm{ad}} = -\begin{pmatrix} 0 & 1 \\ -1 & 0 \end{pmatrix} \frac{W}{\frac{d\Theta_2}{dz}} \partial_z \boldsymbol{X} = \hat{R}_{-\pi/2} \frac{W}{\Theta_2'} \partial_z \boldsymbol{X}\,, \tag{47}$$

with

$$W = \frac{u_\theta}{r}\left(\frac{u_\theta^2}{r} + f u_\theta\right)\,, \tag{48}$$

and the $\hat{R}_{\theta_0}$ indicating rotation by the angle θ. Inserting (47) into the explicit expressions for the field $\boldsymbol{\Psi}$ that arises in the centerline equation of motion in (3), one turns the terms describing the centerline evolution (see Eq. 90 in Appendix E) into a linear differential operator acting on $\boldsymbol{X}$. The latter can be interpreted as the Hamiltonian of a (complex-valued) Schrödinger equation (54) that leads to a purely real-valued spectrum, i.e., to precession of the centerline in the complex $(x - y)$ plane.

The diabatic motion of the centerline on the other hand results from inserting some non-trivial $\boldsymbol{w}_{1,\mathrm{dia}}$ into $\boldsymbol{\Psi}$ which in our case, for purposes of setting up an elucidating test case for the subsequent comparison of asymptotics and 3D numerics, shall be a rotated version of (47):

$$\boldsymbol{w}_{1,\mathrm{dia}} = \hat{R}_{\theta_0} \frac{W}{\frac{\mathrm{d}\Theta_2}{\mathrm{d}z}} \partial_z \boldsymbol{X}\,. \tag{49}$$

Here θ_0 is the relative orientation of the diabatic vertical velocity dipole relative to the tilt. Clearly, $\boldsymbol{w}_{1,\mathrm{dia}}$ coincides with $\boldsymbol{w}_{1,\mathrm{ad}}$ for $\theta_0 = -\pi/2$. Therefore, such a diabatic heating vertical velocity pattern will result in an additional contribution to the centerline motion of the same orientation and magnitude as the adiabatic contribution. By numerical experiments we observed that the adiabatic vertical velocity dipole, oriented $-\pi/2$ relative to the tilt leads to a centerline motion in the direction $+\pi/2$.

In contrast, by varying θ_0 we expect a diabatic centerline forcing which is oriented $-\theta_0$ relative to the tilt. Therefore, for our formulation of diabatic heating the rotation angle θ_0 determines whether the diabatic forcing leads to acceleration ($\theta_0 = -\pi/2$) or deceleration ($\theta_0 = \pi/2$) of the centerline precession or to increasing ($\theta_0 = \pi$) or decreasing the tilt of the centerline. Note in this context that the resulting linear operator governing the diabatic centerline motion effectively is the rotated version of the adiabatic operator (multiplied with complex number on the unit circle), i.e., its spectrum is rotated in complex plane as $\boldsymbol{w}_1$ is rotated. Real parts of the spectrum lead to precession while imaginary parts lead to growth/damping of the centerline amplitude.

In the further course of diabatic experiments we make use of our findings and specify heating patterns of the form

$$\boldsymbol{Q}_{1,\theta_0} := \frac{\mathrm{d}\Theta_2}{\mathrm{d}z} \boldsymbol{w}_{1,\mathrm{dia}} = \hat{R}_{\theta_0} W \partial_z \boldsymbol{X}. \tag{50}$$

6 Comparison between asymptotic model and three-dimensional simulations

In the course of this paper we presented the derivation of a system of partial differential equations (PDEs) governing the leading-order dynamics of a tilted tropical cyclone in weak cyclostrophic regimes on time scales slow compared with the vortex turnover time (1 and 3).

The aim of this section is twofold: First, we intend to validate the reduced model equations against the three-dimensional Euler equations, i.e., the relevant first principle equations (5), by solving both sets of equations in a suitable numerical framework. To this end, we follow the work of Papke [25] who presented the first results on this scenario. The second goal is to highlight principal mechanisms that are activated by purely asymmetric heating. Therefore, after analyzing the adiabatic dynamics of an initially tilted vortex in an environment without external wind shear ($\boldsymbol{u}_s = 0$), we continue by constructing an idealized asymmetric diabatic heating pattern which will be imposed on the vortex under different angles relative to the tilt. We will refer to these experiments as *adiabatic* (reference simulation), *stagnation*, *intensification* and *attenuation* according to their influence on tilt and centerline geometry.

The quasi-two-dimensional Eqs. (1) and (3) are solved by a combination of appropriate numerical methods, details of which are presented in Appendix F. For the three-dimensional simulations the general purpose atmospheric flow model EULAG (see, e.g., [29,42]) provides efficient integration strategies for the compressible Euler equations (5), and EULAG's compressible mode was used here. These two alternative representations of the tilted vortex flows will be referred to as *asymptotic* and *three-dimensional* simulations.

Note that, although we worked out the scaling in the cyclostrophic regime ($\mathrm{Ro} = \mathscr{O}(1/\delta)$) above, the vortex initial data adopted in the following sections are in the gradient-wind regime ($\mathrm{Ro} = \mathscr{O}(1)$) because we are principally interested in mechanisms active in the course of storm-to-hurricane transition. Therefore, in the numerical treatment terms involving the Coriolis parameter $f_{\mathrm{ref}} = 7.3 \times 10^{-5}$ 1/s, even if reasonably small, will not be neglected.

6.1 Numerical setting and initial data

According to the asymptotic analysis, a tilted vortex that is initially balanced w.r.t. acoustic and internal waves evolves on a slow time scale that is comparable to the synoptic time scale as discussed by Päschke et al. [26]. Higher-order dynamics occurs in the presence of initial perturbations (excitation of higher-order asymptotic modes) on faster time scales. However, we are interested in the leading-order effects only, and thus we construct initial data to closely reproduce the leading-order symmetries assumed in the asymptotic analysis of Sect. 3. This should allow us to obtain solutions following—qualitatively speaking—the evolution on the slow manifold of precessing quasi-modes.

For both, the asymptotic model and EULAG, it is crucial to have a notion of a balanced background state. Prescribing the background potential temperature

$$\bar{\Theta}(z) = T_{\mathrm{ref}} \, \exp\left(\frac{N_{\mathrm{ref}}^2}{g} z\right), \tag{51}$$

we find the background density $\bar{\rho}$ and pressure $\bar{p}$ by integrating the hydrostatic equation with boundary value $\bar{p}(z=0) = p_{\mathrm{ref}}$ and making use of the dimensional form of (5e):

$$\bar{p} = p_{\mathrm{ref}} \left(\frac{R\bar{\rho}\bar{\Theta}}{p_{\mathrm{ref}}}\right)^{\gamma}. \tag{52}$$

To motivate the construction of initial data, we are considering the case of an adiabatic vortex for which (1) is trivially stationary,

$$\frac{\partial}{\partial t} u_\theta^{(0)} = 0, \tag{53}$$

and the centerline equation (3) becomes a Schrödinger-type equation,

$$i\,\partial_t X = \hat{H} X, \tag{54}$$

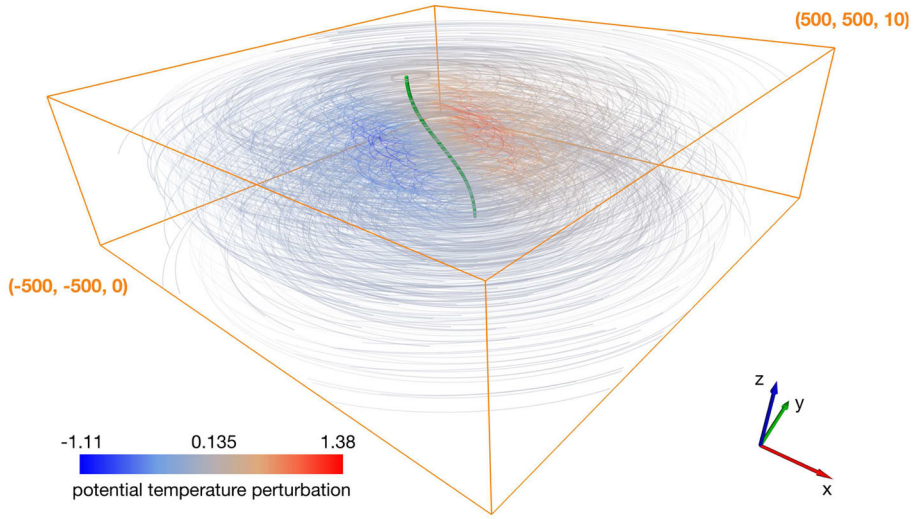

Fig. 3 Initial setup of an idealized tropical cyclone with tilted centerline. The displayed domain is zoomed in to 500 km × 500 km × 10 km. The centerline (bold green) indicates the center at each height around which the flow circulates (visualized by streamlines). In the inner domain, streamlines are shaded (colorized) according to the value of the potential temperature perturbation. To mitigate with initial imbalances, the data shown here is the result of initial data constructed by Eqs. (54) through (59), which subsequently ran freely for 4 days in EULAG (color figure online)

with a Hamiltonian $\hat{H}$ depending on the tangential velocity $u_\theta(r, z)$ and the z-dependent background profiles $\bar{\rho}$, $\bar{p}$, $\bar{\Theta}$. Note, that we have introduced $X := (\boldsymbol{X} \cdot \boldsymbol{i}) + i(\boldsymbol{X} \cdot \boldsymbol{j})$ as the complex representation of $\boldsymbol{X}$ (see Appendix E). With suitable boundary conditions $\hat{H}$ takes the form of a Sturm–Liouville operator and therefore exhibits a real-valued, discrete spectrum [43], which sets the precession frequency of each eigenmode. The first non-trivial eigenvalue corresponds to the slowest varying solution and comes with a *cosine-like* eigenfunction [26] as the simplest time dependent solution with a non-trivial vortex tilt. Related details are omitted here but can easily be validated by numerical means.

As tilt is crucial for coupling asymmetric diabatic heating modes to the leading-order vortex dynamics, we prescribe an initially barotropic tangential velocity profile

$$u_\theta(r) = q_m \frac{1 - e^{-\sigma^2 r^2}}{2\sigma^2 r}\,, \tag{55}$$

corresponding to a Gaussian vorticity profile

$$q(r) = q_m e^{-\sigma^2 r^2}, \tag{56}$$

with q_m and σ chosen such that

$$u_\theta(r = R_{\mathrm{mw}}) = u_{\theta,\max} = u_{\mathrm{ref}} \tag{57}$$

and

$$\frac{\partial}{\partial r} u_\theta(R_{\mathrm{mw}}) = 0\,, \tag{58}$$

where $R_{\mathrm{mw}} = 100$ km. Note that the radial velocity profile (55) results in a *barotropic* velocity distribution for an untilted vortex, only. The vertical displacement due to the centerline tilt renders the flow field genuinely baroclinic.

We take the first non-trivial eigenfunction of $\hat{H}$ to define the initial centerline geometry, scaled to a displacement of 160 km, as depicted by the bold(green) curve in Fig. 3 and arrange the tangential flow profile with respect to the centerline (see streamlines in Fig. 3).

For compliance with the rigid wall horizontal and vertical boundary conditions imposed by EULAG, and to avoid spurious wave reflections near the boundary of the computational domain, the velocity initial data

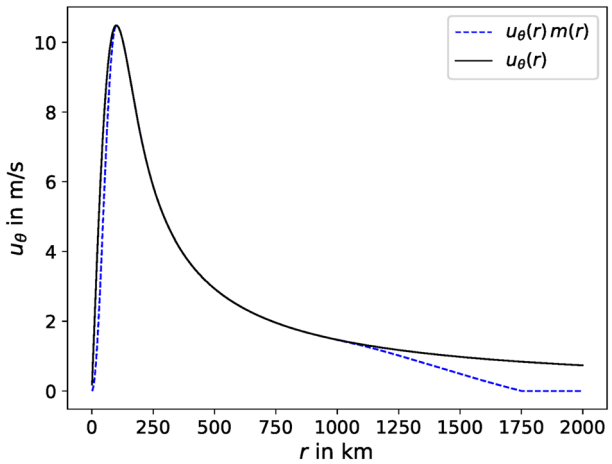

Fig. 4 Radial profile of initial tangential velocity. Solid line corresponds to the unmodified profile (55) and the dashed line to the profile after applying the mollifier (see 59)

for the three-dimensional simulations are smoothly transitioned to zero at some finite radius by applying a mollifier:

$$m(r) = \begin{cases} \sin^2\left(\frac{\pi}{2}\frac{r}{r_0}\right), & r < r_0 \\ 1, & r_0 < r < r_1 \\ \cos^2\left(\frac{\pi}{2}\frac{r-r_1}{r_1-r_\infty}\right), & r_1 < r < r_\infty \\ 0, & r > r_\infty\,. \end{cases} \tag{59}$$

Here $r_1 = 1\,250$ km and $r_\infty = 1\,750$ km are the radii at which the mollifier starts and where it reaches full-suppression, respectively. In addition, the profile within $r_0 = 100$ km is adjusted to preserve differentiability at the origin. Although somewhat arbitrary, the choice of r_1 and r_∞ is based on the sensitivity of tilt and tangential velocity toward these parameters. Tests (not presented here) yield that the solution remains essentially unchanged until decreasing both radii by a factor of $\sim$5. Thus, larger radii of the mollifier seem not to affect the vortex at all. Hence, we argue that the above choice is reasonable under the considerations of avoiding interactions with the domain boundary as well as essentially capturing the far-field behavior of the vortex. The resulting radial profile of initial tangential velocity is displayed in Fig. 4. (Anticipating the forthcoming discussion in Sect. 6.2.1, we note that r_1 and r_2 are both larger than the so-called critical radius [31]).

Section 4.1 yields higher-order diagnostic expressions $u_r^{(2)}$, $u_\theta^{(2)}$, $w^{(0)}$, $\rho^{(4)}$, $p^{(4)}$, and $\Theta^{(4)}$, which we have used to achieve higher-order balance. An example is shown in Fig. 3 by colorizing streamlines with the potential temperature perturbation. The dipolar perturbation is negative in the tilt direction and positive up-tilt.

In the three-dimensional case the vortex is embedded into a domain of 4000 km extent in both horizontal directions, 10 km in the vertical, and a damping layer surrounds the domain near the horizontal boundaries to suppress gravity waves emerging from the inner core and to keep them from reflecting. The thickness of the layers is 500 km, and the characteristic damping time scale is set to $\tau = 10^4$s, a setting that has proven to absorb internal waves resulting from small imbalances of the initial data.

In line with the structural properties of the tropical cyclone, i.e., an inner core with a smooth transition to the quasi-geostrophic far field, we use the static mesh refinement capability of EULAG [29] and map equidistantly spaced coordinates onto a grid focused at the inner core. The actual mapping is accomplished by

$$\begin{pmatrix} x_p \\ y_p \end{pmatrix} = c_1 \begin{pmatrix} x_c \\ y_c \end{pmatrix} + c_2 \begin{pmatrix} x_c^\alpha \\ y_c^\alpha \end{pmatrix}\,, \tag{60}$$

where $\alpha = 5$, $c_{1,2} = 1/2$. $(x, y)_{p,c}$ are normalized coordinates on the domain $[-1, 1]^2$. Figure 5 demonstrates how the horizontal grid is focused toward the center of the computational domain.

The asymptotic equations are solved on a regular equidistant tilted polar grid on the domain $(r, z) \in [0, 1.12] \times [0, 12.5]$ in dimensionless units covering roughly a tilted cylinder of 1000 km around the centerline and the full vertical extent of 10 km.

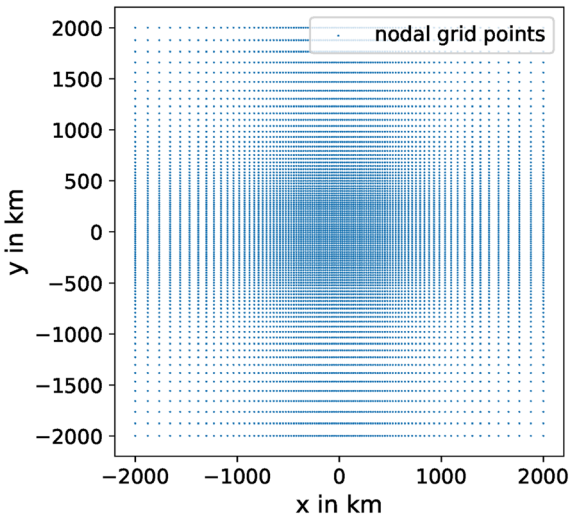

Fig. 5 Horizontal structure of stretched grid used for solving the three-dimensional Euler equation with EULAG

In the further course, we will compute the diabatic heating from Eq. (50) which involves the reconstruction of both, the current centerline position and circumferentially averaged tangential velocity. For the first, we borrow one of the concepts described by Nguyen et al. [21] and define the center of mass of the vorticity field at each horizontal level as

$$\boldsymbol{X}(t,z) = \int \boldsymbol{k}\cdot(\nabla\times\boldsymbol{u}_{||}(t,\boldsymbol{x},z))\boldsymbol{x}\ \mathrm{d}^2\boldsymbol{x}\,. \tag{61}$$

This formula is evaluated here utilizing a second-order accurate discretization outlined by Papke [25]. The circumferential mean of u_θ then is computed by the Biot–Savart integral

$$u_{\theta,0}(r,z) = \frac{\Gamma(r,z)}{2\pi r} = \frac{1}{2\pi r}\int\limits_{B_r(\boldsymbol{X}(z))} \boldsymbol{k}\cdot(\nabla\times\boldsymbol{u}_{||}(t,\boldsymbol{x},z))\ \mathrm{d}^2\boldsymbol{x}\,, \tag{62}$$

where $B_r(\boldsymbol{X}) = \{\boldsymbol{x}_{||}\in\mathbb{R}^2|(\boldsymbol{x}_{||}-\boldsymbol{X})^2 < r^2\}$ denotes the circular domain centered at $\boldsymbol{X}$ with radius r.

Remark We have adopted here a Gaussian initial vorticity profile (cf. 56) which guarantees that the vorticity decays rapidly outside the vortex core in gradient wind balance. As a consequence, the vortices do not exhibit self-alignment due to critical damping of vortex Rossby waves as discussed in ([31,40], and references therein), because the vorticity and its gradient are exponentially small in terms of the perturbation parameter δ at the critical radius. The mollifier (59) does not change this circumstance. This choice allows us to focus in this work on changes in vortex tilt and intensity due to diabatic effects only. See also Sect. 7 for a discussion of critical damping in relation to the present theory.

6.2 Results and discussion

Here we present results of numerical simulations solving either the full three-dimensional Euler equations (5) or the reduced asymptotic equation (1) for the primary circulation velocity $u_\theta^{(0)}$, and the centerline evolution (3). More information regarding the numerical methods used, including empirical convergence tests, is provided in Appendices E to G.

6.2.1 Adiabatic vortex

As a reference for the following experiments we first investigate the dynamics of a tilted adiabatic vortex. In Sect. 6.1 we constructed initial data to follow the first non-trivial eigenmode of the governing (adiabatic)

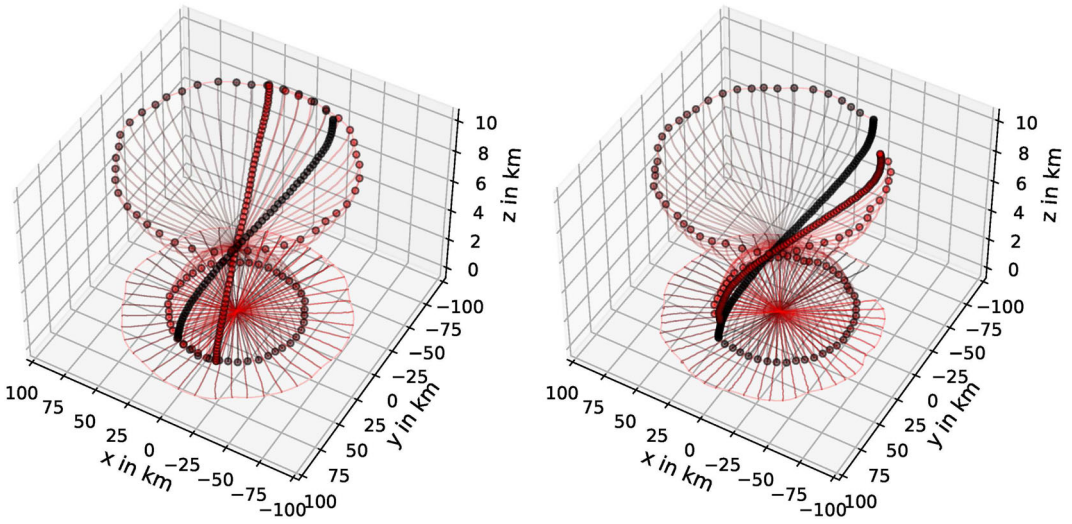

Fig. 6 Time evolution of centerline for an adiabatic vortex for 6 days. Shown are the results of the asymptotic (left) and the three-dimensional simulation (right). In both panels shading (coloring) of the centerline transits from black to grey (red) indicating counterclockwise precession. Initial ($t = 0$) and final ($t = 6$ days) are highlighted with circle markers along the vertical extent of the centerline. The top and bottom endpoints of the centerline are marked with circles of the respective shading (color) for each timestep. In addition, the centerline is projected onto the bottom surface (color figure online)

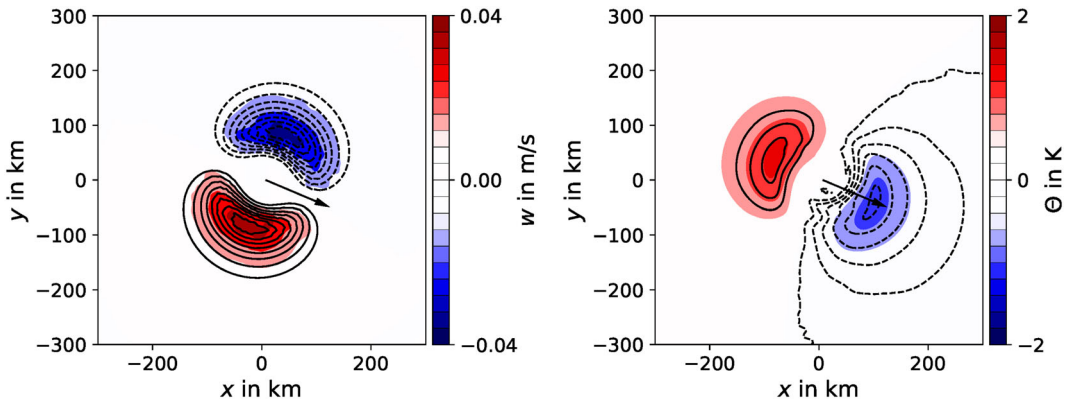

Fig. 7 Horizontal slices of vertical velocity (left) and potential temperature (right). Color shades depict the numerical results at 5000 m height and 1.5 days with values ranging from -0.04 to 0.04 $\mathrm{m/s}$ in steps of 0.004 $\mathrm{m/s}$ (left) and from -2 to 2 K in steps of 0.2 K with positive (red) and negative (blue) sign. Contour lines correspond to the asymptotic prediction (solid for positive and dashed for negative sign). The arrow indicates position and tilt direction of the centerline (color figure online)

Hamiltonian, and we found stationarity of the mean tangential wind according to (53). Hence, from the structure of (54) we expect undamped precession of this eigensolution.

Figure 6 compares the results of the three-dimensional and asymptotic adiabatic simulations with initial data as discussed. Though exhibiting some small-scale oscillations and damping, the three-dimensional simulation (Fig. 6, right panel) compares well with its asymptotic analogue. Time scales of one precession are 5.5 days for the asymptotic and 6.5 days for the three-dimensional simulation. This difference leads to a deviation of the final positions of the centerline but given that the effective expansion parameter $\delta = \sqrt{\varepsilon} \sim 1/3$, this is well within the error bounds of the leading-order solution.

The asymptotic analysis revealed non-trivial leading-order gradient-wind (cyclostrophic) and hydrostatic balances for the vertical velocity w and for the thermodynamic quantities depending on the centerline tilt. In Fig. 7 both, w and $\tilde{\Theta}$ are visualized by a representative horizontal slice at 5000 m at $t = 1.5$ days comparing asymptotic values (black contours) with the 3D numerical simulation results (shaded/color-coded). The tilt vector $\partial_z \boldsymbol{X}$ is indicated by an arrow. Qualitative similarities are rather apparent, while deviations are again well within the asymptotic truncation order $\mathscr{O}(\delta) \sim 1/3$. Both figures demonstrate the alignment of dipolar

perturbations relative to the tilt as $\boldsymbol{w}_1$ and $\boldsymbol{\Theta}_1^{(4)}$ are rotated by $-90°$ and $180°$, respectively. Jones [10] found similar patterns for vortices tilted by externally imposed shear.

We emphasize that the amplitude of the three-dimensional representation of the vertical velocity dipole $\boldsymbol{w}_1$ is weaker compared to the asymptotic one (0.37 m/s vs. 0.40 m/s in the present case of Fig. 7) which could, at least partially, explain the deviation of precession time scales found in Fig. 6. Reasons for that may be found in the discretization scheme of EULAG introducing special numerical viscosity [29].

Remarkably, due to the fact that the primary circulation velocity, $u_\theta^{(0)}$, is time independent in the adiabatic case, the asymptotic problem reduces to linear Hamiltonian dynamics with time independent coefficients. The time evolution of the entire flow field is nevertheless nonlinear because of the alignment of the vortex within the solution-dependent tilted cylindrical coordinates. Whereas we can superimpose two centerline solutions of the homogeneous centerline equation to obtain a third one for given $u_\theta^{(0)}$, we cannot not do so for the associated entire flow fields because the superimposed leading-order velocity would not be axisymmetric with respect to the superimposed centerline.

Furthermore, readers familiar with earlier studies on vortex resilience against vertical shear (see, e.g., [31,33]) may appreciate an assessment of the importance of resonance damping in the present case. This mechanism can stabilize a vortex against vertical shear and induces vertical self-alignment in an unsheared environment. It relies on a resonance between vortex precession and the propagation of vortex Rossby waves which arises at the critical radius. At this radius, the turn-over time associated with the primary circulation matches the period of the vortex precession. The strength of the damping is a function of the radial gradient of (potential) vorticity at the critical radius. The present set-up is based on the Gaussian-shaped vorticity distribution from (55) with $\sigma = 1/94.5\,\mathrm{km}$. The critical radius lies at $r_{\mathrm{cr}} \approx 950\,\mathrm{km}$, so that $\exp(-\sigma^2 r_{\mathrm{cr}}^2) \approx e^{-100}$, and with it the radial gradient of vorticity, is extremely small. Therefore, the resonance damping mechanism is not active in the present case.

6.2.2 Stagnation

The stagnation test follows the idea that the choice of $\theta_0 = \pi/2$ for the diabatic heating pattern (50) leads to deceleration of the centerline precession by canceling the term $\boldsymbol{\Psi}$ in (3). Furthermore, such a heating structure has no impact on the leading-order tangential velocity: With purely asymmetric heating, the terms involving the axisymmetric vertical and radial motions $u_{r,00}$ and w_0 vanish identically and the tangential velocity time evolution becomes

$$\frac{\partial u_\theta}{\partial t} = -u_{r,*}\left(\frac{u_\theta}{r} + f\right). \tag{63}$$

Considering that $u_{r,*}$ is the projection of the diabatic heating onto the tilt vector,

$$u_{r,*} = \frac{1}{2}\left(\partial_z \boldsymbol{X} \cdot \boldsymbol{Q}_{1,\pi/2}\right) = \frac{1}{2}\left(W\,\partial_z \boldsymbol{X} \cdot \left(\hat{R}_{\pi/2}\partial_z \boldsymbol{X}\right)\right) = 0\,, \tag{64}$$

we realize that the right-hand side of (63) vanishes, too, due to orthogonality of $\partial_z \boldsymbol{X}$ and $\hat{R}_{\pi/2}\partial_z \boldsymbol{X}$.

By construction, inserting the heating $\boldsymbol{Q}_{1,\pi/2}$ into (37) also satisfies $\boldsymbol{w}_1 \equiv 0$ to leading order. Figure 8 shows the expected behavior for the three-dimensional simulations. $\boldsymbol{Q}_{1,\pi/2}$ attenuates the vertical velocity by a factor of $1/5 \approx 0.66\,\delta$, i.e., it eliminates the leading-order dipole of w visible in the left panel of Fig. 7. The residual depicted in the right panel of the present Fig. 8 is thus the result of higher-order asymptotic contributions and, possibly, additional numerical truncation errors. Our main point here is that with the cancellation of the circumferential Fourier mode one of the vertical velocity, both the influence of tilt and heating onto the vortex strength as represented by $u_{r,*}^{(2)}$ in (34) and the self-induced vortex motion due to Ψ explained in Sect. 5.4, vanish identically. These conclusions are supported by the time independence of the primary circulation strength seen in Fig. 9 and by the substantial slow-down of the centerline precession in Fig. 10, respectively.

As discussed above, the leading-order tangential velocity is not affected by asymmetric heating of the given orientation. Figure 9 presents both the time series of maximum tangential wind (dark/blue) and of maximum heating (light/red). Only small variations in the tangential velocity are apparent and, as we will see in the next subsection, this changes substantially when we alter the orientation of $\boldsymbol{Q}_{1,\theta_0}$.

Experiments (not shown here) revealed instabilities caused by small perturbations due to discretization errors: The diabatic heating will exhibit large amplitudes where the local tilt $\partial_z \boldsymbol{X}$ (being result of the reconstruction (61)) is large. This affects the local velocity and as a consequence the spectral properties of the

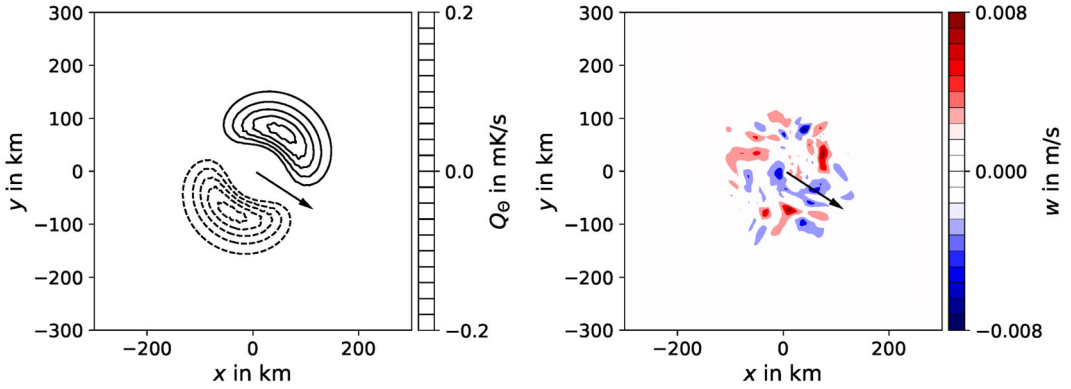

Fig. 8 Asymmetric heating pattern in stagnating configuration with orientation of $\theta_0 = \pi/2$ relative to the tilt (left) and residual vertical velocity (right) on a horizontal slice at 5000 m and 1.5 days. Left: Contour lines represent absolute values from 0.02 to 0.12 mK/s in steps of 0.02 mK/s. Right: Color shades represent absolute values up to 0.008 m/s with positive (red) and negative (blue) sign(color figure online)

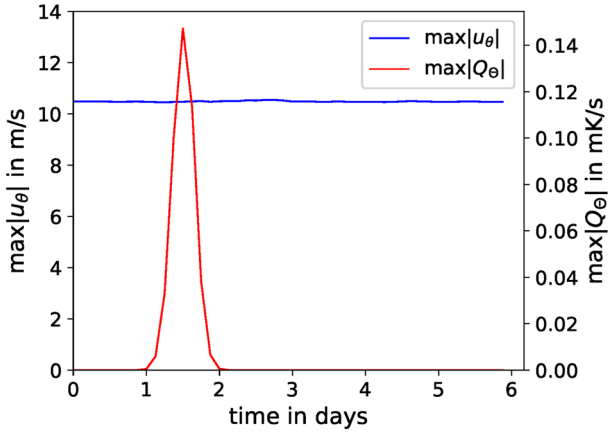

Fig. 9 Time series of maxima of mean tangential wind (62) (dark/blue) and diabatic heating pattern (50) (light/red) in the stagnation configuration. As predicted by the theory, no significant impact on the mean tangential wind is observed(color figure online)

Hamiltonian of Eq. (54) (projecting onto higher frequency modes) increasing small-scale oscillatory features of the centerline $\boldsymbol{X}$. Hence, we need make sure to maintain a certain regularity of $\boldsymbol{X}$ to avoid obscuring the effect under consideration by triggering this feedback loop. We achieve this by restricting the heating to a concentrated pulse by applying a time-dependent amplitude factor of the shape

$$f(t) = a \exp\left(\frac{(t-b)^2}{2c^2}\right) \tag{65}$$

For the current setting $a = 1$, $b = 1.5$ days and $c = \frac{1\text{day}}{2\sqrt{2\ln 300}}$.

Note that the proportionality of the heating strength to the vortex tilt mentioned above is an artifact of the present idealized choice of a heating pattern, which was not chosen to be realistic, but serves the purpose of testing our hypotheses. When latent heat release from convection will replace the present heating structure in subsequent studies, we expect a more robust response.

The heating distribution $\boldsymbol{Q}_{1,\pi/2}$ constructed in such a way guarantees $u_{r,*}$ to vanish (cf. 64) and by canceling $\boldsymbol{w}_1$, the term involving the vector $\boldsymbol{\Psi}$ is cancelled from the centerline equation of motion (3). As discussed in the introduction of Sect. 6, we are initially in the regime of gradient-wind balance. Hence, $\boldsymbol{M}_1$ remains the only contribution to the centerline equation of motion. Numerical evaluations show that the amplitude of $\boldsymbol{M}_1$ is about 1/6 of the amplitude of the $\boldsymbol{\Psi}$ in the adiabatic case which is why we observe a significant slowdown of the centerline precession in the asymptotic case in Fig. 10, left panel, during the heating time interval (cf. Fig 6 for reference). Although not as prominently as with the asymptotic simulation due, likely, to the

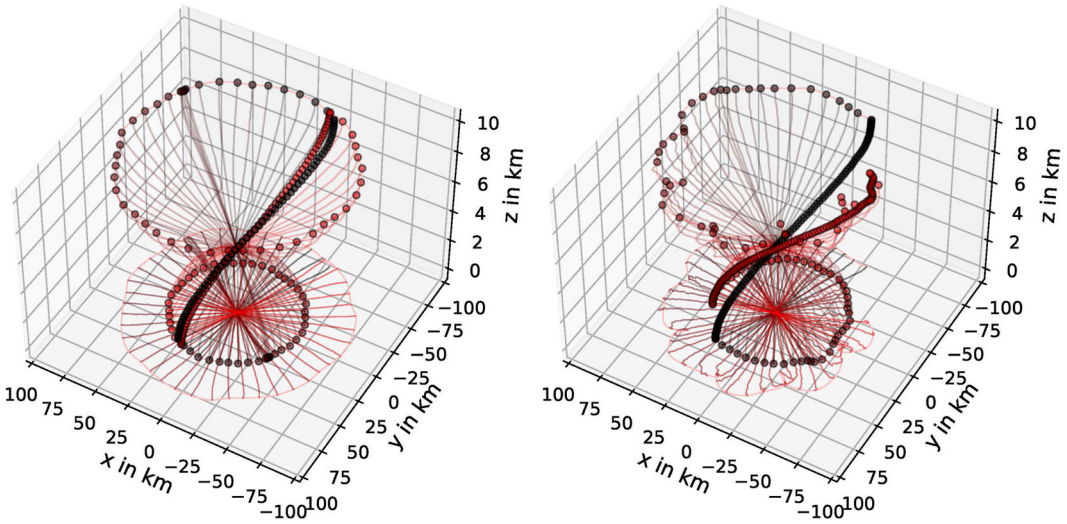

Fig. 10 Same as Fig. 6 but for a vortex under the influence diabatic heating (stagnation case with $\theta_0 = \pi/2$). Left: asymptotic solution for 6 days with diabatic heating applied between day 1 and 2 slowing down the precession speed. Right: three-dimensional reference simulation with same heating parameters

aforementioned discretization errors, the centerline also slows down in the three-dimensional simulation. It also becomes transparent that, due to the heating, the shape of the centerline acquires short-wavelength features that are excited due to a slight misalignment of the diabatic heating dipole.

6.2.3 Intensification

In Sect. 5.4 we constructed a dipolar heating pattern and, by aligning its orientation $\theta_0 = \pi/2$ relative to the centerline tilt, we found stagnation, i.e., deceleration of the centerline precession as well as suppression of the vortex-induced vertical velocity dipole. However, what is the influence of this heating dipole when oriented with $\theta_0 = \pi$ relative to the tilt? $\theta_0 = \pi$ determines the sign of (64) to be negative and as a consequence the right-hand side of (63) positive, i.e., leading to intensification. To examine the effect of the orientation of a dipolar heating pattern without altering its amplitude by the dependency of $\boldsymbol{Q}_{1,\theta_0}$ on u_θ and $\partial_z \boldsymbol{X}$ we fix u_θ and $|\frac{\partial \boldsymbol{X}}{\partial z}|$ in (50) to values at $t = 1$ day but still keep track of the orientation of $\frac{\partial \boldsymbol{X}}{\partial z}$.

In contrast to Fig. 9, where we did not see any sizeable impact of diabatic heating on the mean circumferential velocity, Fig. 11 displays a clear increase for both the asymptotic and three-dimensional equations. We notice that the intensification is more effective for the asymptotic simulation ($\sim$ 3 m/s) than it is for the three-dimensional simulation ($\sim$ 1.5 m/s), even though the heating amplitude of the asymptotic simulation is tuned to meet the three-dimensional simulation. This may be caused by insufficiencies of the centerline reconstruction method used for the three-dimensional simulations ultimately leading to non-optimal alignment of the heating dipole.

From the discussion in Sect. 5.4 we concluded that a heating pattern with orientation $\theta_0 = \pi$ causes the centerline tilt to increase. This behavior is found valid in the current experiment as seen in Fig. 12. Both simulation approaches, asymptotic and three-dimensional, exhibit stretching of the centerline during the phase of active heating. Since the increase in tangential velocity is not as efficient for the three-dimensional simulation as it is for the asymptotic counterpart, after the period of heating, the centerline precesses with higher angular frequency in the asymptotic case. Again, this may be due to inaccuracies in the three-dimensional simulation when computing and aligning the heating dipole.

In Sect. 5.2 we discussed the intensification/attenuation mechanism as result of the effective vertical velocity dipole resulting from the superposition of both adiabatic and diabatic contributions. In the current situation the diabatic vertical velocity dipole is oriented by $\theta_0 = \pi$ while the adiabatic dipole is oriented by $-\pi/2$. Both are of comparable amplitude, hence, we expect an angle of $-3\pi/4$ between tilt and resulting vertical velocity which is verified by results shown in the right panel of Fig. 13.

Although the intensification is rather weak, there is evidence that the orientation of the asymmetry of the diabatic heating matters for the evolution of the circumferential velocity. In fact, by allowing for stronger

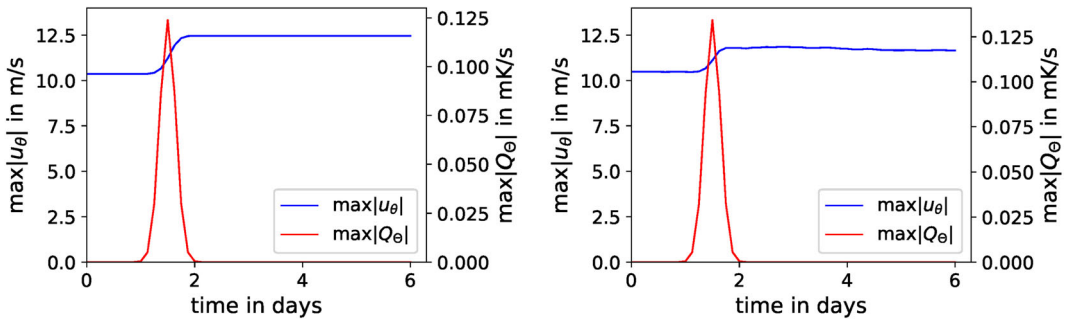

Fig. 11 Same as Fig. 9 with $\theta_0 = \pi$ (intensifying configuration) for both approaches, asymptotic (left) and three-dimensional (right). The circumferential wind is increased by $\sim$ 3 m/s and $\sim$ 1.5 m/s due to the anti-parallel alignment of the diabatic heating for the asymptotic and three-dimensional simulation, respectively (color figure online)

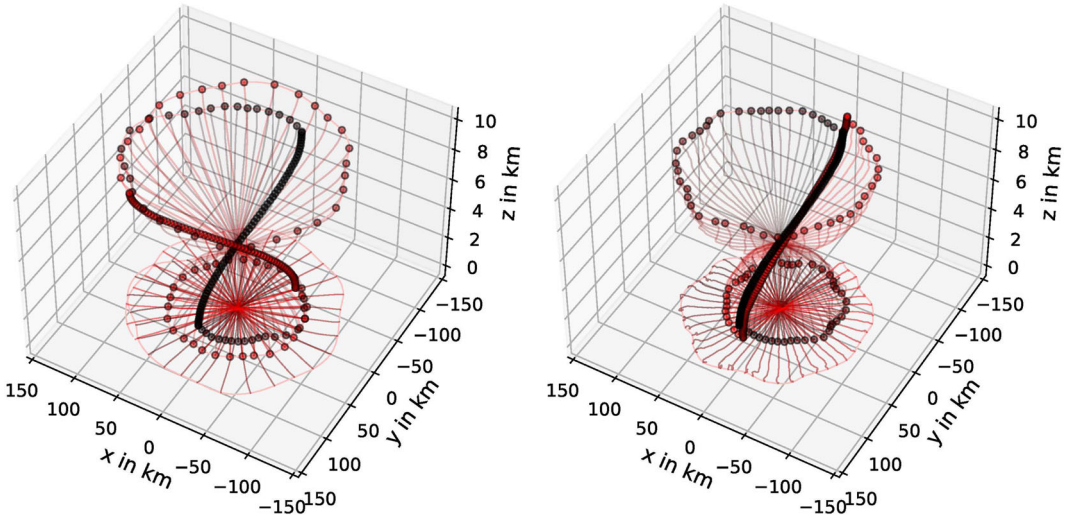

Fig. 12 Same as Fig. 10 with $\theta_0 = \pi$ (intensification configuration)

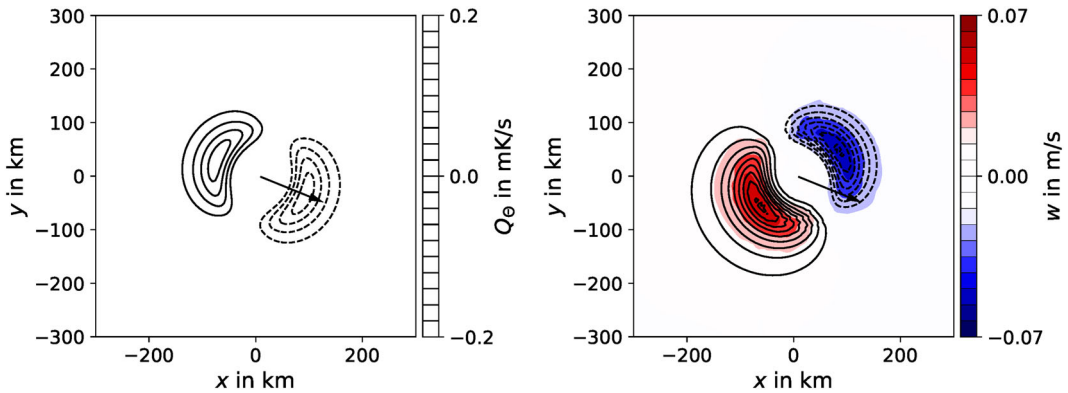

Fig. 13 Same as Fig. 8 with $\theta_0 = \pi$ (intensification configuration) (color figure online)

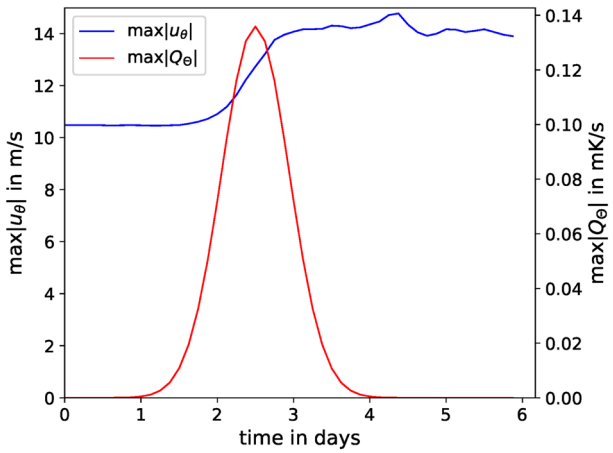

Fig. 14 Same as Fig. 11, right panel, for the three-dimensional intensification experiment with $\theta_0 = \pi$ and an extended heating phase between day 1 and 4 (color figure online)

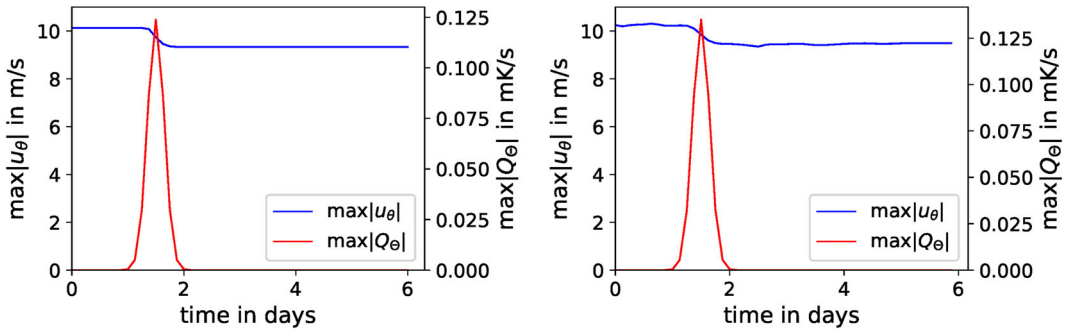

Fig. 15 Similar to Fig. 11, $\min_z \max_{x,y} u_\theta$ is shown for the attenuating configuration ($\theta_0 = 0$) for both approaches, asymptotic (left) and three-dimensional (right). In both cases, the circumferential wind is decreased by ~ 1 m/s due to the parallel alignment of the diabatic heating (color figure online)

heating by increasing the duration of the heat pulse the effect on the tangential velocity is stronger (see Fig. 14), but it also affects the structure of the centerline in a more profound manner.

6.2.4 Attenuation

The final experiment of this work consists in switching the heating dipole pattern to a configuration where we expect attenuation of the vortex and vertical alignment of the centerline. Following Eq. (64) attenuation corresponds to $\theta_0 = 0$, i.e., positive heating in the direction of the centerline tilt. Again, tilt amplitude and tangential velocity of Eq. (50) are set to values at $t = 1$ day to avoid non-linear feedback and restricted by an amplitude factor to act over a short interval only.

Taking into account that initially, the velocity profile has uniform vertical structure in the tilted polar coordinate system (r, z), and that the heating dipole is constructed such that it lowers the tangential velocity mainly in regions at mid-altitude, whereas regions above and below remain essentially unaffected, straightforward evaluation of the global maximum of u_θ would not be insightful. To remedy this issue, in Fig. 15 we plot the quantity

$$u_\theta^{mm} = \min_z \max_{r,\theta} u_\theta \tag{66}$$

as a proxy for the intensity change of the vortex. Both simulation approaches show the reduction in tangential wind speed due to asymmetric diabatic heating, now in remarkable congruence.

Finally, in Fig. 16 both, asymptotic and three-dimensional simulations show how the centerline aligns when forced by the attenuating heating. In the same way as before, we see small deviations in the precession time

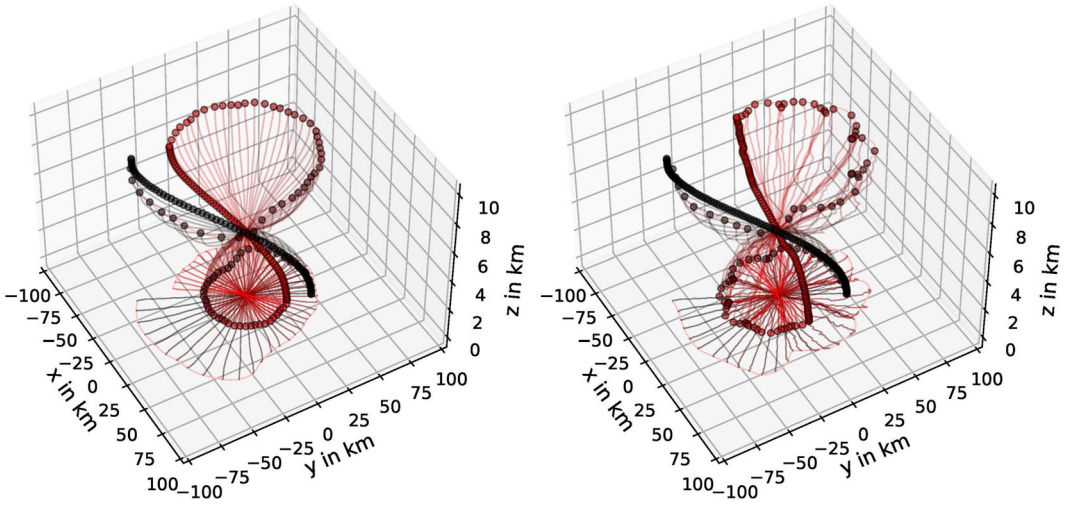

Fig. 16 Same as Fig. 10 with $\theta_0 = 0$

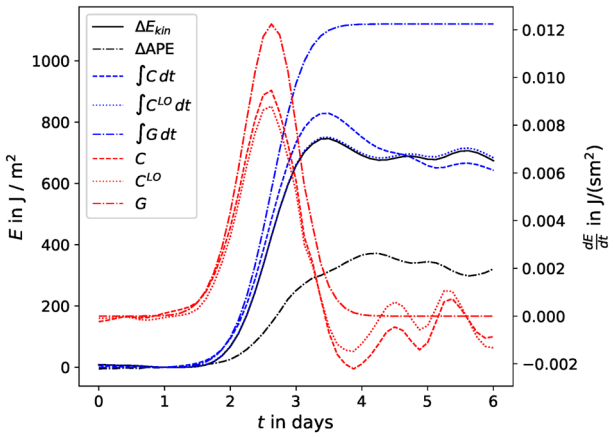

Fig. 17 Differential and integral energy contributions for the extended intensification experiment according to the APE theory of Lorenz [14]. Blue lines represent time series of the domain-integrated energy contributions of the source terms G (APE generation), C (conversion rate to kinetic energy), and C^{LO} (asymptotic leading-order approximation of C). For comparability reasons all energy-like quantities (blue and black) are shifted by a constant to pass the point (1 day, 0), i.e., to follow the graph of ΔE_{kin}

scale and excitation of higher-order oscillatory modes but otherwise good agreement between the asymptotic and three-dimensional experiments.

6.3 Energetics of asymmetric diabatic heating

In this section we want to analyze the energy budget of the vortex in some more detail following the theory on available potential energy (APE) by Edward Lorenz. To this end, we shall consider the seminal work of Lorenz [14] who includes a detailed account of why only part of the generation of potential energy by diabatic heating is available for conversion into kinetic energy. He provides explicit expressions for the total APE generation, G, and its conversion into mechanical energy, C, as a function of the current flow state and the diabatic heating rates. The relevant formulae are provided in Appendix D, Eqs. (76c) and (76d), respectively, and it is shown there how we use (85), (87e), and (88) to numerically evaluate these expressions in the present Cartesian coordinate system while Lorenz works with pressure coordinates.

We begin by analyzing the extended intensification experiment presented in Sect. 6.2.3. Figure 17 shows energy rates of change, in red with the scale on the right, and the corresponding time integrated amounts of energy, in blue with the scale on the left of the diagram. The solid black line reveals the increase in total kinetic

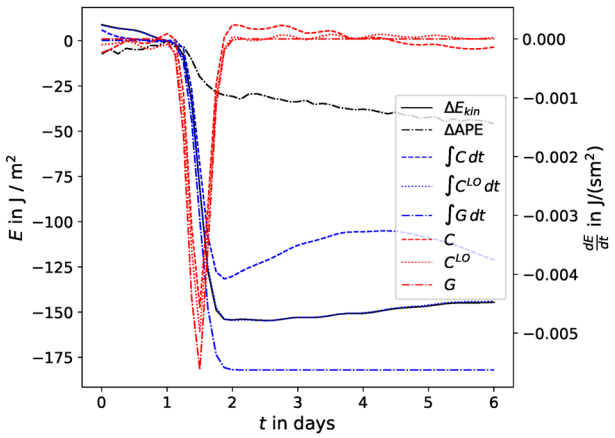

Fig. 18 Same as Fig. 17 with $\theta_0 = 0$ (attenuation configuration)

energy, ΔE_{kin}, whereas the dash-dotted black line (both with the scale on the left) shows the accumulation of APE, labeled ΔAPE in the figure. Both are defined as the difference between time t and some reference time, here $t_0 = 1$ day. The analysis demonstrates that the system's kinetic energy increases as a consequence of the imposed asymmetric heating in line with our findings of Sect. 5.3. Furthermore, APE accumulation amounts to about one third of the total generation of APE which is seen in the dash-dotted blue curve. This scaling is consistent with the asymptotic results which state that the accumulation of APE should be small of $\mathscr{O}(\delta)$, with $\delta = \sqrt{\varepsilon} \sim 1/3$ in the present case.

The dash-dotted and dashed blue curves represent $\int G \, \mathrm{d}t$, the total generation of APE, and $\int C \, \mathrm{d}t$, the total conversion into kinetic energy. The corresponding rates, G and C, computed by the formulae (85) and (87e), are shown as the dash-dotted and dashed red curves, respectively. Appendix D shows that, to leading order in the asymptotics, C obeys the same expression as G when one relates the vertical velocity to the diabatic heating rate via the weak temperature gradient approximation (cf. 85 and 88b). For a more detailed comparison, Fig. 17 also shows the leading-order asymptotic expression for the conversion rate, C^{LO} (dotted, red), which is evaluated on the basis of (88a) in Appendix D. Interestingly, one obtains this formula for the APE conversion rate from that for the total generation rate by replacing the heating-related term $\frac{Q_\Theta}{\partial\overline{\Theta}/\partial z}$ in the expression for G with the vertical velocity w from the 3D simulation. This corresponds to replacing the leading-order asymptotic result for w in (35) (see 119 for the general expression in physical dimensions) with the vertical velocity generated in the full 3D dynamics.

Figure 17 shows that C^{LO} approximates C rather well throughout the entire 6 days. In fact, it does so much better than one may expect from an $\mathscr{O}(\delta)$ asymptotic truncation error. Furthermore, the time integrated change of kinetic energy, ΔE_{kin}, and $\int C^{\text{LO}} \, \mathrm{d}t$ are practically equal as one may expect from Lorenz' theory, i.e., $\dot{E}_{\text{kin}} \simeq C^{LO}$. Finally, the difference between total APE generation, $\int G \, \mathrm{d}t$, and kinetic energy change, ΔE_{kin}, approximately equals the accumulated APE, ΔAPE, that is, $\frac{\mathrm{d}}{\mathrm{d}t}\text{APE} \approx G - C$ as postulated by Lorenz, see (76a).

These findings primarily confirm, that the generation and conversion of APE are equal up to leading order (remember that $\delta \approx 0.3$). Next they reveal that APE does accumulate at first order and that the amount of APE accumulation is accounted for by the difference between G and C^{LO}. The only difference in the formulae used to evaluate these two quantities is that the vertical velocity w in (88a) is either evaluated by its leading-order asymptotic approximation in (119) (for G) or taken directly from the 3D simulation (for C^{LO}), respectively. The fact that only C^{LO}, using w from the simulation, closely reproduces the time derivative of kinetic energy suggests that the actual vertical motions are the central driver for the observed intensification rather than the heating itself. G on the other hand, assuming that Q_Θ is translated into vertical motions via (119) introduces an offset which is accounted for by creating APE. Hence, the difference is caused by deviations from the weak temperature gradient approximation which is satisfied only at leading order. Further evidence is gained by considering the tail of C (or C^{LO}) for $t > 4$ days. Even without diabatic heating, conversion between APE and kinetic energy continues as the energy, intermediately stored in APE and essentially accounting for imbalances, now is getting converted (back and forth) to and from kinetic energy mediated by the vertical motions.

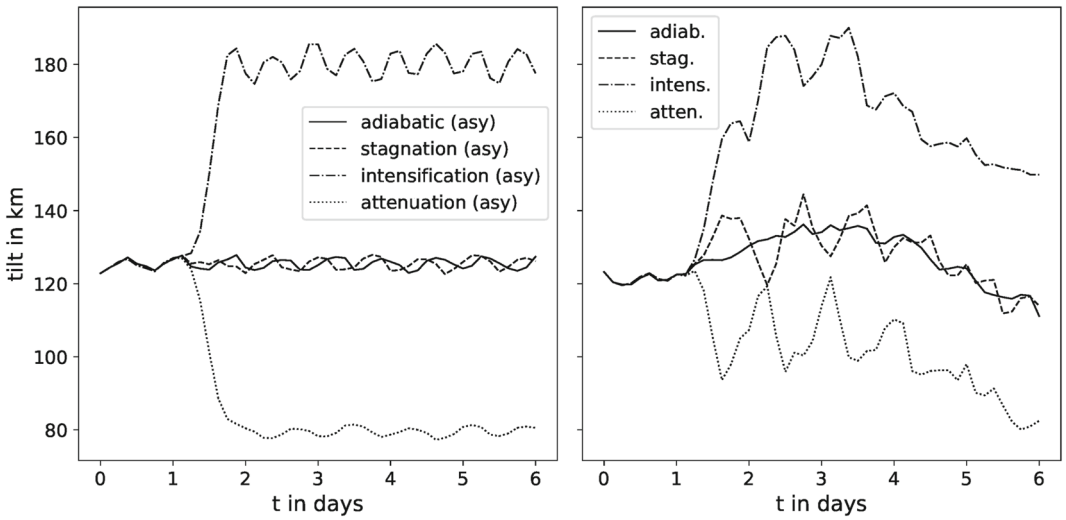

Fig. 19 Time series of tilt amplitudes for asymptotic (left) and three-dimensional (right) experiments. Both panels range over the same time period, but the three-dimensional simulations are preceded by 4 days of initial balancing

In addition, similar to the intensification experiment (cf. Fig. 17), Fig. 18 demonstrates the reduction in integrated kinetic energy due to the attenuating configuration of the heating dipole. In contrast to the previous experiment, we now find almost perfect agreement of all conversion rates and consequently the impact ΔAPE is negligible. This once more reveals the stable nature of this configuration driving the vortex toward the solution of zero tilt and zero velocity.

Remark (item 5): These considerations lead us to conclude that it is not the diabatic heat release which is primarily important for changes in kinetic energy but the resulting vertical motions and their correlation with temperature perturbations rooted in the structure of the tilted vortex. This settles our statement posed in the introduction in item 5.

6.4 Summary of tilt dynamics

As a final result, we present a quantitative analysis of the effect of asymmetric diabatic heating on the centerline tilt by considering the time series of tilt amplitude as measured by an L_2-norm:

$$\left\| \frac{\partial \boldsymbol{X}}{\partial z} \right\| := \int_0^{z_{\text{top}}} \left(\sqrt{\frac{\partial \boldsymbol{X}}{\partial z} \cdot \frac{\partial \boldsymbol{X}}{\partial z}} \right) \mathrm{d}z, \qquad z_{\text{top}} = 10 \text{ km}. \tag{67}$$

In Fig. 19 this quantity is plotted for all types of experiments performed in the course of this work (except the extended intensification experiment). The left graph shows the results from the evaluations of the asymptotic theory, and it confirms that the orientation of the diabatic heating dipole correlates with changes in the tilt amplitude. Aligning the heating dipole with the tilt (attenuation case) leads to decreasing tilt, i.e., the vortex tends to align vertically. This situation turns around if the heating dipole is rotated by 180° (intensification case) in that the tilt further increases. Although in the stagnation configuration (heating dipole is 90 degrees rotated relative to the tilt) neither the primary circulation nor the tilt magnitude are affected by the heating/cooling pattern, the centerline precession is slowed down during the period of active heating/cooling as predicted by the theory.

The graph on the right in Fig. 19 reveals that the three-dimensional representation of the initial data does not project as well onto the first eigenmode of the centerline as in the asymptotic cases. Besides features which oscillate on a time scale of less than one day, all three-dimensional simulations exhibit an additional systematic trend on the scale of roughly six days. However, in every case, asymptotic and three-dimensional, the effects of activating an asymmetric diabatic heating dipole are superimposed onto the adiabatic reference. The stagnation simulation follows the adiabatic reference on both cases but exhibits slight distortions in the

three-dimensional case. As discussed before, this is the reason for restricting the diabatic heating to a short time period as this effect would increase for longer periods. However, for both experiments, intensification and attenuation, the tilt amplitude follows approximately the adiabatic reference curve albeit on increased and lowered levels, respectively, once the short time period heating activity has passed.

We argue that the response to asymmetric diabatic heating in the three-dimensional simulations is not as direct as it is for the asymptotic analog simulations. This is probably due to imbalances excited through the diabatic heating, e.g., by misalignment of the heating dipole, and limits the efficacy of the heating in (50) in influencing tilt and circumferential velocity. Nonetheless, in all cases the intensification configuration increases the centerline tilt while the attenuation configuration decreases it.

Remark (items 3 and 6): The analysis of this section corroborates our initial statement in (item 3) of the introduction which implies that the orientation of a purely dipolar diabatic heating pattern intensifies and shears an atmospheric vortex apart in the anti-parallel orientation of heating dipole and tilt while it attenuates and aligns the vortex vertically in the parallel orientation. They also justify our claim in (item 6) that the predictions of the asymptotics are fully corroborated at a qualitative level by three-dimensional simulations. As regards quantitative discrepancies, these are largely within the expected error of just a leading-order asymptotic solution with values of the expansion parameter $\delta \sim 1/3$.

7 Conclusions and outlook

With the present work we have extended the results of Päschke et al. [26] to vortex Rossby numbers larger than unity corresponding to wind speeds of $\mathcal{O}(30\ \mathrm{m/s})$ and showed that the principal structure of the reduced asymptotic model equations is retained in this limit. We found that the validity of the equations holds from the gradient-wind regime up to (modest) cyclostrophic vortices. This corresponds to hurricanes of strength H1 on the Saffir-Simpson scale.

Current models of tropical cyclone intensification rely on organized symmetric heating in an upright vortex [[20], and references therein]. Observations show, however, that in incipient tropical storms the level of organization of convection is weak compared to that in fully developed hurricanes so that, in the former, patterns of convection can be strongly asymmetric relative to the nearly axisymmetric primary circulation. Our findings of leading-order effects of asymmetric diabatic heating on both the strength of the primary circulation and on the vortex tilt may therefore add new insights into possible routes of acceleration from tropical storms to fully developed hurricanes.

Here, we have focused on highlighting the potential effect of *purely asymmetric* diabatic heating on the mean tangential velocity for an initially tilted vortex. This effect, we argued, can be of the same order of magnitude in the presence of strong vortex tilt as that of symmetric diabatic heating. Although the gain of horizontal wind speed was limited in our three-dimensional simulations as we restricted to idealized heating configurations that maintain the overall flow structure which the asymptotic analysis was based on, we expect to see potentially stronger efficiencies in nature due to the self-regulation of moist convection in a sheared environment.

The effects of moist thermodynamics have been replaced here by artificial diabatic source and sink terms neglecting effects of water phase transitions. As we argued, the resulting asymmetric pattern of vertical velocity is the driver for the intensification/attenuation mechanism found in this study. In ongoing research, to be published elsewhere in the future, we find that mean vertical mass fluxes of an ensemble of convective towers can provide for similar effects. In fact, the heating-induced vertical velocities from the present study would be replaced in this case by convective mass fluxes averaged over an ensemble of convective towers, while the rest of the theory remains largely unchanged. Thus, despite its somewhat artificial setup, the present study does reveal a potentially interesting physical mechanism.

In this work we did not discuss the interaction of environmental shear with the TC. However, observations of TCs just before rapid intensification often show a phase of relatively stationary configuration of background wind shear [39], vortex tilt, and asymmetries of convection [41]. In this situation, regions of strong convection develop down-shear left from the vortex center [4,32]. Taking into account that the shear-induced vortex tilt will lead to precession of the vortex in counter clock-wise direction until shear and self-induced precession tend to cancel each other [33,44], we find that a down-shear left position of convection is at the same time close to down-tilt. Such a convection pattern will decompose into a mean axisymmetric and purely asymmetric components, the latter dominated by the first azimuthal Fourier mode. The symmetric part of the heating will, according to the present study (depending on the radial positioning of the heating center relative to the RMW),

tend to accelerate the vortex, while it potentially aligns the centerline, i.e., reduces the tilt due to vertical advection (see second term on the right in Eq. 105). In contrast, the first Fourier asymmetric mode, according to the mechanism discussed in this paper, contributes an attenuating trend to the primary circulation while (also) working to reduce the tilt and thus to efficiently stabilize the vortex against the outer shear (see Sect. 6.2.4 and Fig. 16). In this scenario, which is in line with a situation described by Wang and Holland [44], a sudden break-down of the outer shear will interrupt the attenuating effect of the asymmetric part of convection (that depends on the tilt) leaving the field to the symmetric and intensifying part. In addition to stabilization due to asymmetric diabatic heating, self-alignment due to critical damping [31,40] can play an important role in that scenario, depending on the vortex' vorticity distribution. The result is a potential pathway for rapid intensification, to be studied in detail in future work.

Critical damping of vortex Rossby waves has been identified as one mechanism responsible for the observed resilience of atmospheric vortices against tilting by background shear and for their capability of vertical (re-)alignment (see [31,40], and references therein). Critical damping arises when, at some radius, the rotation rate of a linear perturbation eigenmode of the vortex matches with the local angular velocity associated with its primary circulation. To address this phenomenon within the framework of the present theory, two regimes must be distinguished. In the first regime, the critical radius lies in the far field QG region, in the second within the gradient wind vortex core. In the first case, critical damping should be accessible within the present theoretical framework, and it will arise as part of the outer QG flow solution. To this end, the inner solution for the vortex core in gradient wind balance should be combined with the critical layer theory for nearly axisymmetric quasi-geostrophic vortices of Reasor and Montgomery [30] as the outer solution. This should be interesting material for one future study. To address the second case, for which the critical radius lies within the gradient wind part of the vortex, a more sophisticated asymptotic approach is needed: In this case, the angular velocity of the primary circulation at the critical radius is comparable to the vortex turn over time scale, which is much faster than the time scale of the QG outer flow considered exclusively in the present work. To simultaneously capture the combined dynamics on both time scales, techniques of multiple scales asymptotics will have to be invoked. This could give rise to a second interesting future study.

Ongoing research aims to extend the asymptotic theory to include realistic moist process sub-models and multiscale convection. In this context, the present observations regarding the net effects of vertical motions (see discussion of Fig. 15) will become important in that mean convective mass fluxes will take the role of the present heating-induced vortex-scale vertical velocities. Another interesting avenue for future research will be a thorough thermodynamic analysis of the heating/convection–tilt interactions in the spirit of, e.g., Pauluis and Zhang [27].

Acknowledgements T.D., A.P., and R.K.'s work has been funded by Deutsche Forschungsgemeinschaft (DFG) through grant CRC 1114 "Scaling Cascades in Complex Systems", Project Number 235221301, Project (C06) "Multi-scale structure of atmospheric vortices", and by the Helmholtz Society of Research Institutions for funding through the "GeoSim" Graduate College. The authors also thank the European Centre for Medium Range Weather Forecast for supporting this work by R.K's ECMWF research fellowship as well as hosting T.D., A.P., and R.K. for research stays. The authors acknowledge the North-German Supercomputing Alliance (HLRN) as well as the German Climate Computing Center (DKRZ) for providing HPC resources that have contributed to the research results reported in this paper. The authors also gratefully thank Olivier Pauluis, Remi Taullieux, and Mike Montgomery for many fruitful discussions which have helped strengthen our interpretation of the asymptotic results. T.D. and R.K. further thank Sundararaman Gopalakrishnan, Frank Marks, Paul Reasor, and Dave Nolan for their hospitality and insightful discussions during a research stay at NOAA/HRD and University of Miami in the spring of 2019. NCAR is sponsored by the National Science Foundation. Finally, the authors express their gratitude to the two anonymous reviewers who helped to forge the final version of this paper through their challenging, yet fruitful questions and remarks.

Funding Open Access funding enabled and organized by Projekt DEAL.

Declarations

Conflicts of interest The authors declare that they have no conflict of interest.

Code availability Computational codes and their setups needed to rerun the calculations presented in this work are available from the authors upon reasonable request.

Authors' contributions Tom Dörffel, Ariane Papke, and Rupert Klein are responsible for the study conception and design. The computational code for solving the asymptotic limit model was developed by Tom Dörffel, adaptation of the EULAG solver and its post-processing engine to the test cases was pursued by Ariane Papke and Tom Dörffel supported at critical stages by Piotr Smolarkiewicz, data analysis and display was were performed and realized by Tom Dörffel and Natalia Ernst, and the interpretation and evaluation of the results was in the hands of Tom Dörffel, Rupert Klein, and Piotr Smolarkiewicz. The first draft of the manuscript was written by Tom Dörffel and all authors commented on intermediate versions of the manuscript. All authors read and approved the final manuscript.

Funding This research has been funded by Deutsche Forschungsgemeinschaft (DFG) through grant CRC 1114 'Scaling Cascades in Complex Systems, Project Number 235221301, Project C06 'Multiscale structure of atmospheric vortices'.

Availability of data and material Not applicable, as the codes for reproduction of the evaluated simulation data are made available.

A Governing equations in the co-moving coordinates

Transforming (5) to the vortex-centered coordinates from Sect. 3.2 using (19) and defining $\boldsymbol{U} \equiv \delta\, \partial \boldsymbol{X}/\partial t$ and $\boldsymbol{u}_{\mathrm{rel}} = u_r\, \boldsymbol{e}_r + u_\theta\, \boldsymbol{e}_\theta$ we find

$$\frac{\partial(\boldsymbol{U}+\boldsymbol{u}_{\mathrm{rel}})}{\partial \widehat{t}} + \frac{1}{\delta}\boldsymbol{u}_{\mathrm{rel}}\cdot\widehat{\nabla}\boldsymbol{u}_{\mathrm{rel}} + \frac{w}{\delta^3}\left[\frac{\partial}{\partial z} - \frac{\partial \boldsymbol{X}}{\partial z}\cdot\widehat{\nabla}\right](\boldsymbol{U}+\boldsymbol{u}_{\mathrm{rel}}) + \frac{1}{\delta^7}\frac{1}{\rho}\widehat{\nabla}p + \frac{1}{\delta^2} f\,\boldsymbol{k}\times(\boldsymbol{U}+\boldsymbol{u}_{\mathrm{rel}}) = 0, \tag{68a}$$

$$\frac{\partial w}{\partial \widehat{t}} + \frac{1}{\delta}\boldsymbol{u}_{\mathrm{rel}}\cdot\widehat{\nabla}w + \frac{w}{\delta^3}\left[\frac{\partial}{\partial z} - \frac{\partial \boldsymbol{X}}{\partial z}\cdot\widehat{\nabla}\right]w + \frac{1}{\delta^{10}}\left(\frac{1}{\rho}\left[\frac{\partial}{\partial z} - \frac{\partial \boldsymbol{X}}{\partial z}\cdot\widehat{\nabla}\right]p + 1\right) = 0, \tag{68b}$$

$$\frac{\partial \rho}{\partial \widehat{t}} + \frac{1}{\delta}\widehat{\nabla}\cdot(\rho\boldsymbol{u}_{\mathrm{rel}}) + \frac{1}{\delta^3}\left[\frac{\partial}{\partial z} - \frac{\partial \boldsymbol{X}}{\partial z}\cdot\widehat{\nabla}\right](\rho w) = 0, \tag{68c}$$

$$\frac{\partial \Theta}{\partial \widehat{t}} + \frac{1}{\delta}\boldsymbol{u}_{\mathrm{rel}}\cdot\widehat{\nabla}\Theta + \frac{w}{\delta^3}\left[\frac{\partial}{\partial z} - \frac{\partial \boldsymbol{X}}{\partial z}\cdot\widehat{\nabla}\right]\Theta = Q_\Theta. \tag{68d}$$

B Full second-order horizontal momentum balances

$$\frac{u_\theta^{(0)}}{\widehat{r}}\frac{\partial u_r^{(2)}}{\partial\theta} - \frac{2u_\theta^{(0)}u_\theta^{(2)}}{\widehat{r}} - \frac{(u_\theta^{(1)})^2}{\widehat{r}} + \boldsymbol{e}_\theta\cdot\frac{\partial \boldsymbol{X}^{(0)}}{\partial z}\frac{w^{(0)}u_\theta^{(0)}}{\widehat{r}} + \frac{1}{\rho_0}\frac{\partial \widehat{p}^{(6)}}{\partial \widehat{r}} - \frac{\rho_1}{\rho_0^2}\frac{\partial \widehat{p}^{(4)}}{\partial \widehat{r}} - f_0\, u_\theta^{(1)} = 0 \tag{69a}$$

$$\frac{\partial u_\theta^{(0)}}{\partial t} + w^{(0)}\frac{\partial u_\theta^{(0)}}{\partial z} + u_r^{(2)}\left(\frac{\partial u_\theta^{(0)}}{\partial \widehat{r}} + \frac{u_\theta^{(0)}}{\widehat{r}}\right) + \frac{u_\theta^{(0)}}{\widehat{r}}\frac{\partial u_\theta^{(2)}}{\partial\theta} - w^{(0)}\boldsymbol{e}_r\cdot\frac{\partial \boldsymbol{X}^{(0)}}{\partial z}\frac{\partial u_\theta^{(0)}}{\partial \widehat{r}} + \frac{1}{\rho_0\widehat{r}}\frac{\partial \widehat{p}^{(6)}}{\partial\theta} = 0 \tag{69b}$$

C Derivation of the kinetic energy budget (45)

We start from (43), which is equivalent to (4.21) in [26] for $f_0 = 0$. This is verified straightforwardly by using $u^{(2)}_{r,0} = u^{(2)}_{r,00} + u^{(2)}_{r,*}$. The equation is multiplied by $\widehat{r}\rho_0 u^{(0)}_\theta$, and we use the mass conservation law in the form of Eq. (40), i.e.,

$$\left(\widehat{r}\rho_0 u^{(2)}_{r,00}\right)_{\hat{r}} + \left(\widehat{r}\rho_0 w^{(0)}_0\right)_z = 0\,, \tag{70}$$

to generate the advective transport terms of kinetic energy in conservation form. We let

$$e_\mathrm{k} = \rho_0 {u^{(0)}_\theta}^2/2 \tag{71}$$

and obtain

$$(\widehat{r}e_k)_t + \left(\widehat{r}u^{(2)}_{r,00}e_\mathrm{k}\right)_{\hat{r}} + \left(\widehat{r}w^{(0)}_0 e_\mathrm{k}\right)_z = -\widehat{r}\left(u^{(2)}_{r,00} + u_{r,*}\right)\frac{\partial p^{(4)}}{\partial \widehat{r}}\,. \tag{72}$$

Focusing on the right-hand side of this equation, we rewrite the first term as

$$\begin{aligned}\widehat{r}u^{(2)}_{r,00}\frac{\partial p^{(4)}}{\partial \widehat{r}} = \left(\widehat{r}u^{(2)}_{r,00}p^{(4)}\right)_{\hat{r}} + \left(\widehat{r}w^{(0)}_0 p^{(4)}\right)_z - \widehat{r}\rho_0 w^{(0)}_0\left(\frac{p^{(4)}}{\rho_0}\right)_z \\ -\frac{p^{(4)}}{\rho_0}\left[\left(\widehat{r}\rho_0 u^{(2)}_{r,00}\right)_{\hat{r}} + \left(\widehat{r}\rho_0 w^{(0)}_0\right)_{\hat{r}}\right].\end{aligned} \tag{73}$$

The square bracket vanishes according to (70), while we observe that by combining the axisymmetric part of the hydrostatic balance in (30) with the equation of state in (33) to replace $(p^{(4)}/\rho_0)_z$, and (35) to replace $w^{(0)}_0$ one finds

$$\widehat{r}\rho_0 w^{(0)}_0\left(\frac{p^{(4)}}{\rho_0}\right)_z = \widehat{r}\rho_0\frac{Q^{(0)}_{\Theta,0}}{\mathrm{d}\Theta_2/\mathrm{d}z}\frac{\widehat{\Theta}^{(4)}_0}{\Theta_0}\,. \tag{74}$$

Next we rewrite the second term on the right of (72) using the definition of $u^{(2)}_{r,*}$ in (34), and the first Fourier modes of the vertical momentum balance in (36) to find

$$\widehat{r}u^{(2)}_{r,*}\frac{\partial p^{(4)}}{\partial \widehat{r}} = \frac{1}{2}\widehat{r}\rho_0\,\boldsymbol{w}_1\cdot\frac{\boldsymbol{\Theta}^{(4)}_1}{\Theta_0} = \frac{1}{2}\widehat{r}\rho_0\,\frac{\boldsymbol{Q}^{(0)}_{\Theta,1}}{\mathrm{d}\Theta_2/\mathrm{d}z}\cdot\frac{\boldsymbol{\Theta}^{(4)}_1}{\Theta_0}\,. \tag{75}$$

To obtain the second equality we have used the asymmetric WTG law from (37) and the fact that the second term in that equation contributes a component to $\boldsymbol{w}_1$ that is orthogonal $\partial \boldsymbol{X}^{(0)}/\partial z$, and thus also orthogonal to $\boldsymbol{\Theta}^{(4)}_1$.
Insertion of (73)–(75) generates the desired equation (45).

D Relation to Lorenz' theory of available potential energy

We want to deepen the insight of the proposed asymmetric diabatic heating mechanism by finding connections to Lorenz' concept of available potential energy (APE) [14]. As we will see, under certain assumptions the kinetic energy generation of Eq (45) is identical to Lorenz' expressions of APE generation and conversion to kinetic energy. To this end, we start with Eqs. (16), (20), (17), (18) of Lorenz [14]:

$$\frac{\mathrm{d}\overline{A}}{\mathrm{d}t} = G - C\,, \tag{76a}$$

$$\frac{\mathrm{d}\overline{K}}{\mathrm{d}t} = C\,, \tag{76b}$$

$$G = \frac{1}{g}\int_0^{p_\mathrm{s}} \frac{\Gamma_d}{\Gamma_d - \overline{\Gamma}}\frac{\overline{T'Q'}}{\overline{T}}\,\mathrm{d}p, \tag{76c}$$

$$C = -\frac{R}{g}\int_0^{p_\mathrm{s}} \frac{1}{p}\overline{T\omega}\,\mathrm{d}p\,. \tag{76d}$$

Here, $\overline{A}$ is the average available potential energy, $\overline{K}$ the mean kinetic energy, C the conversion rate between APE and kinetic energy, G the generation rate of APE (all per unit area), p_s the surface pressure, $\omega = \frac{\mathrm{d}p}{\mathrm{d}t}$ the vertical velocity in pressure coordinates, $\overline{\Gamma} = \frac{\partial \overline{T}}{\partial z}$ the lapse rate of mean temperature, $\Gamma_d = g/c_\mathrm{p}$ the dry-adiabatic lapse rate, $Q = c_\mathrm{p}\pi Q_\Theta$ the diabatic source term with the Exner pressure $\pi = \frac{T}{\Theta} = \left(\frac{p}{p_\mathrm{ref}}\right)^{R/c_p}$, $\overline{(\cdot)}$ the horizontal mean on constant-pressure surfaces, and $(\cdot)'$ the deviation from the mean. In our case we neglect friction, hence Eq. (21) of Lorenz [14] is trivially zero.

First, we need to point out that (independently of our asymptotic theory) every quantity $q(x, y, p, t)$ defined as field in pressure coordinates can be expressed as the sum of mean and perturbation,

$$q(x, y, p, t) = \overline{q}(p, t) + q'(x, y, p, t)\,, \tag{77}$$

where trivially $\overline{q'} = 0$. By definition, there are no pressure perturbations on constant-pressure surfaces $p' = \pi' = 0$. This allows us to express Q conveniently as

$$Q = \overline{Q} + Q' = c_p\pi\left(\overline{Q_\Theta} + Q'_\Theta\right)\,. \tag{78}$$

Together with $T'/\overline{T} = \Theta'/\overline{\Theta}$ and assuming the atmosphere to be hydrostatic ($\frac{\partial p}{\partial z} = -g\rho$) we find $\overline{\Gamma} = -\overline{\pi\frac{\partial\Theta}{\partial z}} + \Gamma_d$. The generation rate G becomes

$$G = \int_0^{p_s} \frac{1}{\overline{\frac{\partial\Theta}{\partial z}}}\frac{\overline{\Theta' Q'_\Theta}}{\overline{\Theta}}\,dp\,. \tag{79}$$

This expression involves the integration of horizontal means on surfaces of constant pressure. For comparing this expression with the findings of our asymptotic analysis, with means and perturbations defined on levels of constant height, we consider the following approximation. For some locally defined physical quantity q with representation $q(x, y, p)$ in pressure coordinates, we introduce its representation in Cartesian space coordinates by

$$q^c(x, y, z) = q(x, y, p^c(x, y, z))\,, \tag{80}$$

where $p^c(x, y, z) = Z^{-1}(z; x, y)$, $Z(p; x, y)$ is the geometrical height as a function of pressure as given by the pressure coordinates, and $(\,)^{-1}$ denotes the inversion of the $z \leftrightarrow p$ relationship at frozen horizontal location (x, y). Let furthermore

$$\overline{p^c}(z) \qquad \text{and} \qquad \overline{Z}(p) = \overline{p^c}^{-1}(p) \tag{81}$$

denote the mean pressure on a surface of constant height z and its inversion, respectively. Then, taking into account that pressure fluctuations in horizontal planes are small, we use first-order Taylor expansion in z to obtain

$$\begin{aligned} q(x, y, p) &= q^c\left(x, y, Z(p; x, y)\right) = q^c\left(x, y, \overline{Z}(p) + \left(Z(p; x, y) - \overline{Z}(p)\right)\right) \\ &= q^c\left(x, y, \overline{Z}(p)\right) + \frac{\partial q^c}{\partial z}\left(x, y, \overline{Z}(p)\right)\left(Z(p; x, y) - \overline{Z}(p)\right) + \mathscr{O}\left(Z'^2\right) \\ &= q^c\left(x, y, \overline{Z}(p)\right) + \frac{\partial q^c}{\partial z}\left(x, y, \overline{Z}(p)\right)\frac{p^c\left(x, y, \overline{Z}(p)\right) - p}{\partial p^c/\partial z\left(x, y, \overline{Z}(p)\right)} + \mathscr{O}\left(p'^2\right) \end{aligned}$$

$$= q^c\left(x, y, \overline{Z}(p)\right) - \left(\frac{p'}{g\rho}\frac{\partial q^c}{\partial z}\right)\left(x, y, \overline{Z}(p)\right) + \mathscr{O}\left(p'^2\right) \tag{82}$$

where $Z' = Z(p; x, y) - \overline{Z}(p)$ and, by the definition of $Z(p; x, y)$ given above,

$$p'(x, y, z) = p^c(x, y, z) - p^c\left(x, y, Z(\overline{p^c}(z); x, y)\right) = p^c(x, y, z) - \overline{p^c}(z) \tag{83}$$

is the local pressure fluctuation in the Cartesian system. The findings of Sect. 4 reveal that we can neglect terms of order $\mathscr{O}\left(p'\right)$ and higher at the cost of introducing an error of order $\mathscr{O}\left(q\delta^4\right)$, i.e., about 1% of the magnitude of q. This is a consequence of the fact that pressure is mainly vertically stratified and that the flow is essentially hydrostatic. These considerations justify approximating the average on constant-pressure surfaces $\overline{(\cdot)}$ by

$$\overline{q(x, y, p)} \approx \frac{1}{|\Omega|}\int_{\Omega} q\left(x, y, \overline{Z}(p)\right) \mathrm{d}x\,\mathrm{d}y, \tag{84}$$

where $\Omega \subset \mathbb{R}^2$ is the appropriate surface area to average over. With these results we approximate the total APE generation in (79) by the integrals in Cartesian coordinates, substituting $\mathrm{d}p = -g\rho\,\mathrm{d}z$ to obtain, up to higher-order terms (h.o.t.),

$$G = \int_{\Omega\times[0,\infty]} \frac{g\rho}{\frac{\partial\Theta}{\partial z}} \frac{\Theta' Q'_\Theta}{\Theta}\,\mathrm{d}x\,\mathrm{d}y\,\mathrm{d}z + \text{h.o.t.}\,, \tag{85}$$

now with perturbations on surfaces of constant height. This expression approximates the original formulation (Eq. 76c) without further assumptions on the structure of Q_Θ.
Using the equation of state $p = RT\rho$ in the definition of the APE conversion term C in (76d), we find

$$C = -\frac{1}{g}\int_0^{p_s} \overline{\left(\frac{\omega}{\rho}\right)}\,\mathrm{d}p. \tag{86}$$

This integral gives the source term of (global) kinetic energy production (neglecting friction). $\omega := \frac{\mathrm{d}p}{\mathrm{d}t}$, however, turns out to be difficult in handling numerically if data is given on Cartesian coordinates as it requires tracing pressure changes along fluid trajectories in space and time. For achieving sufficient accuracy rather high temporal resolution would be necessary. We bypass this problem by the following derivation: Assuming a hydrostatic atmosphere this term reads in Cartesian coordinates as

$$C = -\frac{1}{g}\int_0^{p_s} \overline{\left(\frac{\omega}{\rho}\right)}\,\mathrm{d}p = -\frac{1}{|\Omega|}\int_\Omega\int_0^{p_s} \frac{\mathrm{d}p}{\mathrm{d}t}\frac{\mathrm{d}p}{g\rho}\,\mathrm{d}x\,\mathrm{d}y \tag{87a}$$

$$= -\frac{1}{|\Omega|}\int_\Omega\int_0^\infty \left(\frac{\partial p}{\partial t} + \boldsymbol{u}\cdot\nabla_{\shortparallel} p + w\frac{\partial p}{\partial z}\right)\mathrm{d}z\,\mathrm{d}x\,\mathrm{d}y \tag{87b}$$

$$= -\frac{1}{|\Omega|}\int_\Omega\int_0^\infty \left(\left[\frac{\partial}{\partial t}\int_z^\infty g\rho\,\mathrm{d}z'\right] + \boldsymbol{u}\cdot\nabla_{\shortparallel} p - g\rho w\right)\mathrm{d}z\,\mathrm{d}x\,\mathrm{d}y \tag{87c}$$

$$= -\frac{1}{|\Omega|}\int_\Omega\int_0^\infty \left(\left[-g\int_z^\infty \left(\nabla_{\shortparallel}\cdot(\rho\boldsymbol{u}) + \frac{\partial\rho w}{\partial z'}\right)\mathrm{d}z'\right] + \boldsymbol{u}\cdot\nabla_{\shortparallel} p - g\rho w\right)\mathrm{d}z\,\mathrm{d}x\,\mathrm{d}y \tag{87d}$$

$$= -\frac{1}{|\Omega|}\int_\Omega\int_0^\infty \boldsymbol{u}\cdot\nabla_{\shortparallel} p\,\mathrm{d}z\,\mathrm{d}x\,\mathrm{d}y \tag{87e}$$

Here we have used, in this sequence, the hydrostatic p–z transformation and the definition of the material derivative dp/dt (a → b), the (vertically integrated) hydrostatic relation for pressure (b → c), and mass continuity (c → d). Then, the first term under the integral in (87d), owing to Gauß' theorem, vanishes with the surface-to-volume ratio of Ω and is neglected in the sequel, while upon integration in z' the second term cancels the fourth, leading to the final result in (87e) which requires only spatial derivatives at constant time.

To relate (87e) to the asymptotic expression for the source term in the kinetic energy balance equation (45), we observe that the integrand in (87e) is the dimensional form of the r.h.s., $\left(u^{(2)}_{r,00} + u_{r,*}\right) \partial p^{(4)}/\partial \widehat{r}$, of the preliminary version of the kinetic energy balance in (72). Repeating the derivations of the axisymmetric and Fourier mode 1 contributions to this term in (74) and (75), respectively, or using the general asymptotic expression for the vertical velocity in (119), we find

$$C = \frac{1}{|\Omega|} \int\limits_{\Omega\times[0,\infty]} g\,\rho\,\frac{\Theta' w}{\Theta}\,\mathrm{d}x\,\mathrm{d}y\,\mathrm{d}z \tag{88a}$$

$$= \frac{1}{|\Omega|} \int\limits_{\Omega\times[0,\infty]} \frac{g\rho}{\frac{\partial\Theta}{\partial z}}\frac{\Theta' Q_\Theta}{\Theta}\,\mathrm{d}x\,\mathrm{d}y\,\mathrm{d}z. \tag{88b}$$

Note that Q'_Θ appears in the APE generation expression G in (85) as opposed to Q_Θ in the expressions for APE conversion C in (88b). This difference implies an additional contribution to C relative to G which accounts for a coupling to the mean heating $\overline{Q}_\Theta$. In the cases studied here, however, the diabatic heating has zero mean, so that (85) and (88b) match in these cases. We conclude that—at leading order in the asymptotics—there is no accumulation of APE since generated APE is immediately converted into kinetic energy. This establishes the desired link between the asymptotic kinetic energy budget in (45) and Lorenz' APE theory.

E The centerline equation of motion

As preparation for Appendix F we give more details on the centerline equation of motion (3) and provide all the necessary information to close the system of equations (in conjunction with (1)).

We will present the missing terms necessary to close equation (3) in Sect. 7, provide a split into adiabatic and diabatic contributions in Sect. 7 and further deepen the analysis of this equation in Sect. 7 for being able to construct a stable and efficient numerical scheme to solve the asymptotic equations.

E.1 Formulation of Päschke et al. (2012)

In the course of this work we argued that the equations derived by Päschke et al. [26] are valid in the vanishing-Coriolis case, i.e., $f_0 \to 0$. The structure of the equations stays essentially the same, only terms proportional to f_0 are to be dropped.

For completeness below we present the remaining expressions for $\boldsymbol{M}_1$ and $\boldsymbol{\Psi}$ necessary to solve the system (1) and (3):

$$\boldsymbol{M}_1 = \frac{f^2}{4\pi\rho_0\Gamma}\partial_z\left(\frac{\rho_0\Gamma^2}{\Theta'_2}\partial_z\boldsymbol{X}\right) \tag{89}$$

$\boldsymbol{\Psi} = L[\mathscr{K}] = \hat{R}_{\pi/2}L[\mathscr{K}_1]$ depends on the following expressions:

$$\mathscr{K}_1 = \mathscr{H}_1 + \tilde{\mathscr{I}}_1 + \mathscr{J}_1 + \mathscr{Q}_1\,, \tag{90a}$$

$$\mathscr{H}_1 = \partial_r\left(r\boldsymbol{w}_1\partial_z u_\theta\right)\,, \tag{90b}$$

$$\tilde{\mathscr{I}}_1 = \mathscr{I}_1 + H_s(r-1)\frac{1}{r^2}\boldsymbol{I}_1\,, \tag{90c}$$

$$\mathscr{I}_1 = r\left(\zeta + f\right)\boldsymbol{W}_1\,, \tag{90d}$$

$$\boldsymbol{I}_1 = \frac{\Gamma}{2\pi}\hat{R}_{-\pi/2}\boldsymbol{M}_1\,, \tag{90e}$$

$$\mathscr{J}_1 = (\partial_r\boldsymbol{\phi}_1)(r\partial_r\zeta)\,, \tag{90f}$$

$$\mathscr{Q}_1 = (w_0\frac{u}{r} - \partial_r(r w_0\partial_r u_\theta))\partial_z\boldsymbol{X}\,, \tag{90g}$$

where $L[\cdot]$ is an integral operator,

$$L[\mathscr{K}] = \frac{\pi}{\Gamma} \int_0^\infty r\mathscr{K}(r)\,\mathrm{d}r\,, \tag{91}$$

and $\hat{R}_{\theta_0}$ denotes the matrix of two-dimensional rotation by an angle θ_0.

Equations (90a–90g) involve the following expressions,

$$\boldsymbol{W}_1 = -\frac{1}{\rho_0}\partial_z(\rho_0 \boldsymbol{w}_1)\,, \tag{92a}$$

$$w_0 = \frac{Q_0}{\frac{\mathrm{d}\Theta_2}{\mathrm{d}z}}\,, \tag{92b}$$

$$\boldsymbol{w}_1 = \frac{1}{\frac{\mathrm{d}\Theta_2}{\mathrm{d}z}}\left(\boldsymbol{Q}_1 + W\hat{R}_{-\pi/2}\partial_z \boldsymbol{X}\right)\,, \tag{92c}$$

$$W = \frac{u_\theta}{r}\left(\frac{u_\theta^2}{r} + f u_\theta\right), \tag{92d}$$

$$\zeta = \frac{1}{r}\frac{\partial(r u_\theta)}{\partial r}, \tag{92e}$$

$$\boldsymbol{\phi}_1 = -r\int_r^\infty \frac{1}{\bar{r}^3}\int_0^{\bar{r}} \bar{\bar{r}}^2 \boldsymbol{R}_1\,\mathrm{d}\bar{\bar{r}}\,\mathrm{d}\bar{r}\,, \tag{92f}$$

$$\boldsymbol{R}_1 = \boldsymbol{W}_1 + \frac{1}{2}(\partial_r w_0)\partial_z \boldsymbol{X}\,, \tag{92g}$$

which are resolved in terms of u_θ, $\boldsymbol{X}$, Q_0 and $\boldsymbol{Q}_1$. The expressions above give rise to the reformulated equation of centerline motion:

$$\partial_t \boldsymbol{X} = \boldsymbol{u}_s + \frac{1}{2}\ln(\delta)\boldsymbol{k}\times\boldsymbol{M}_1 - L[\mathscr{K}_1]. \tag{93}$$

E.2 Split into diabatic and adiabatic contributions

To reveal more clearly the structure of the centerline evolution equation, we recall the formula (37) for the vertical velocity Fourier modes, which separates diabatic from adiabatic effects. Rewriting this formula in the dipole vector notation we have

$$\boldsymbol{w}_1 = \boldsymbol{w}_{1,\mathrm{dia}} + \boldsymbol{w}_{1,\mathrm{ad}}, \tag{94a}$$

$$\boldsymbol{w}_{1,\mathrm{dia}} = \frac{1}{\frac{\mathrm{d}\Theta_2}{P\mathrm{d}z}}\boldsymbol{Q}_1, \tag{94b}$$

$$\boldsymbol{w}_{1,\mathrm{ad}} = \frac{1}{\frac{\mathrm{d}\Theta_2}{\mathrm{d}z}} W\hat{R}_{-\pi/2}\partial_z \boldsymbol{X} =: \hat{R}_{-\pi/2}\hat{w}\boldsymbol{X}, \tag{94c}$$

and realize that the adiabatic part is a linear (differential) operation on $\boldsymbol{X}$:

$$\hat{w} = \frac{W}{\frac{\mathrm{d}\Theta_2}{\mathrm{d}z}}\partial_z \tag{95}$$

From the equations in the previous subsection we see that by linearity of the expressions in $\boldsymbol{w}_1$ we can assemble $\mathscr{K}$ (and ultimately $\boldsymbol{\Psi}$) by linear superposition of linear operations on $\boldsymbol{X}$ (operators are symbolically denoted by $\hat{}$) and in general nonlinear diabatic expressions.

$\mathscr{H}_1$ then becomes:

$$\mathscr{H}_1 = \mathscr{H}_{1,\mathrm{dia}} + \hat{R}_{-\pi/2}\mathscr{H}\boldsymbol{X} \tag{96a}$$

$$\mathscr{H}_{1,\mathrm{dia}} = \partial_r\left(r\boldsymbol{w}_{1,\mathrm{dia}}\right) \tag{96b}$$

$$\mathscr{H}\boldsymbol{X} = \partial_r\left((\hat{w}\boldsymbol{X})\partial_z u_\theta\right) \tag{96c}$$

We first need to evaluate the expression for $\boldsymbol{W}_1$,

$$\boldsymbol{W}_1 = \boldsymbol{W}_{1,\mathrm{dia}} + \hat{R}_{-\pi/2}\hat{W}\boldsymbol{X} \tag{97a}$$

$$\boldsymbol{W}_{1,\mathrm{dia}} = -\frac{1}{\rho_0}\partial_z(\rho_0\boldsymbol{w}_{1,\mathrm{dia}}) \tag{97b}$$

$$\boldsymbol{W}_{1,\mathrm{ad}} = -\hat{R}_{-\pi/2}\frac{1}{\rho_0}\partial_z(\rho_0\hat{w}\boldsymbol{X}) := \hat{R}_{-\pi/2}\hat{W}_{1,\mathrm{ad}}\boldsymbol{X} \tag{97c}$$

to split $\mathscr{I}_1$ accordingly:

$$\mathscr{I}_1 = \mathscr{I}_{1,\mathrm{dia}} + \hat{R}_{-\pi/2}\hat{\mathscr{I}}\boldsymbol{X} \tag{98a}$$

$$\mathscr{I}_{1,\mathrm{dia}} = r\,(\zeta + f)\,\boldsymbol{W}_{1,\mathrm{dia}} \tag{98b}$$

$$\hat{\mathscr{I}}\boldsymbol{X} = r\,(\zeta + f)\,\hat{W}_{1,\mathrm{ad}}\boldsymbol{X} \tag{98c}$$

Together with $\boldsymbol{M}_1$

$$\boldsymbol{M}_1 = \frac{f^2}{4\pi\rho_0\Gamma}\partial_z\left(\frac{\rho_0\Gamma^2}{\frac{\mathrm{d}\Theta_2}{\mathrm{d}z}}\partial_z\boldsymbol{X}\right) \tag{99a}$$

$$=: \hat{M}\boldsymbol{X} \tag{99b}$$

we get the following split for $\tilde{\mathscr{I}}_1$:

$$\tilde{\mathscr{I}}_1 = \mathscr{I}_{1,\mathrm{dia}} + \hat{R}_{-\pi/2}\hat{\tilde{\mathscr{I}}}\mathbf{X} + H_s(r-1)\frac{1}{r^2}\frac{\Gamma}{2\pi}\hat{R}_{-\pi/2}\hat{M}\mathbf{X} \tag{100a}$$

$$=: \mathscr{I}_{1,\mathrm{dia}} + \hat{R}_{-\pi/2}\hat{\tilde{\mathscr{I}}}\mathbf{X} \tag{100b}$$

Performing the split of $\boldsymbol{R}_1$,

$$\boldsymbol{R}_1 = \boldsymbol{W}_{1,\mathrm{dia}} + \hat{R}_{-\pi/2}\hat{W}\boldsymbol{X} + R_{Q,0}\partial_z\boldsymbol{X}\,, \tag{101a}$$

$$R_{Q,0} = \frac{1}{2}(\partial_r w_0) \tag{101b}$$

$\boldsymbol{\phi}_1$ divides into

$$\boldsymbol{\phi}_1 = \boldsymbol{\phi}_{1,\mathrm{dia}} + \hat{R}_{-\pi/2}\hat{\phi}\boldsymbol{X} + \phi_{Q,0}\partial_z\boldsymbol{X} \tag{102a}$$

$$\boldsymbol{\phi}_{1,\mathrm{dia}} = -r\int_r^\infty \frac{1}{\bar{r}^3}\int_0^{\bar{r}} \bar{\bar{r}}^2\boldsymbol{W}_{1,\mathrm{dia}}\,\mathrm{d}\bar{\bar{r}}\,\mathrm{d}\bar{r} \tag{102b}$$

$$\hat{\phi}\boldsymbol{X} = -r\int_r^\infty \frac{1}{\bar{r}^3}\int_0^{\bar{r}} \bar{\bar{r}}^2\hat{W}\boldsymbol{X}\,\mathrm{d}\bar{\bar{r}}\,\mathrm{d}\bar{r} \tag{102c}$$

$$\phi_{Q,0} = -r\int_r^\infty \frac{1}{\bar{r}^3}\int_0^{\bar{r}} \bar{\bar{r}}^2 R_{Q,0}\,\mathrm{d}\bar{\bar{r}}\,\mathrm{d}\bar{r} \tag{102d}$$

and therefore $\mathscr{J}_1$ into

$$\mathscr{J}_1 = \mathscr{J}_{1,\mathrm{dia}} + \hat{R}_{-\pi/2}\hat{\mathscr{J}}\boldsymbol{X} + \mathscr{J}_{Q,0}\partial_z\boldsymbol{X}\,. \tag{103a}$$

$$\mathscr{J}_{1,\mathrm{dia}} = \partial_r(\boldsymbol{\phi}_{1,\mathrm{dia}})(r\partial_r\zeta) \tag{103b}$$

$$\hat{\mathscr{J}}\boldsymbol{X} = \partial_r(\hat{\phi}\boldsymbol{X})(r\partial_r\zeta) \tag{103c}$$

$$\mathscr{J}_{Q,0} = (\partial_r\phi_{Q,0})(r\partial_r\zeta) \tag{103d}$$

For $\boldsymbol{Q}_1$ we find the simple shorthand

$$\mathscr{Q}_1 = \left(w_0\frac{u}{r} - \partial_r(rw_0\partial_r u)\right)\partial_z\boldsymbol{X} \tag{104a}$$

$$=: \mathscr{Q}_0\partial_z\boldsymbol{X}. \tag{104b}$$

Our final result is identifying three different contributions to $\boldsymbol{\Psi}$, a (generally nonlinear) diabatic term, an advective term, and a linear Sturm–Liouville-type operator acting on $\boldsymbol{X}$:

$$\boldsymbol{\Psi} = L[\mathscr{K}_{1,\mathrm{dia}}] + L[\mathscr{J}_{Q,0}\partial_z\boldsymbol{X} + \mathscr{Q}_0\partial_z\boldsymbol{X}] + R_{-\pi/2}L[\hat{\mathscr{H}} + \hat{\tilde{\mathscr{J}}} + \hat{\mathscr{J}}]\boldsymbol{X} \tag{105}$$

E.3 Characteristic structure of the vortex centerline equation

We continue rephrasing the original centerline tendency equation to further emphasize its structure. By trivially identifying $\mathbb{R}^2$ with $\mathbb{C}$ we symbolically transform two-dimensional vectors $\boldsymbol{a} = (a_x, a_y) \in \mathbb{R}$ to $a = a_x + ia_y \in \mathbb{C}$. Operations such as $(\boldsymbol{k}\times\cdot)$ and $\hat{R}_{\pi/2}$ become multiplications with i. By that we can identify a substructure of the equation to be of Schrödinger-type, and advective contribution and a source term, generally dependent on X, u_θ, and the coordinates (r, z, t) but without any further specification:

$$\begin{aligned} i(\partial_t X + L[(\mathscr{J}_{Q,0} + \mathscr{Q}_0)\partial_z X]) = &-\frac{1}{2}\ln\delta\hat{M}X - L[\hat{\mathscr{H}} + \hat{\tilde{\mathscr{J}}} + \hat{\mathscr{J}}]X \\ &+ iu_s - iL[\mathscr{H}_{Q,1} + \mathscr{I}_{Q,1} + \mathscr{J}_{Q,1}] \end{aligned} \tag{106}$$

By identifying structural components, the centerline equation takes the form

$$i(\partial_t X + A\partial_z X) = \hat{H}X + iQ + iu_s \tag{107}$$

Note that the left-hand sides of Eq. (107) resembles an advection operation while the right-hand side involve linear and non-linear source terms.

Päschke et al. ([26], section 6.2) pointed out that the adiabatic time evolution of the vortex centerline poses an eigenproblem. For that case the (homogeneous) centerline equation in the complex plane is written as

$$i\frac{\partial X_h}{\partial t} = \hat{H}X_h\,. \tag{108}$$

As the spectrum ω_k of $\hat{H}$ is real, (108) can be interpreted as a *Schrödinger-type* equation, hence eigenmodes X_k precess with the angular frequency ω_k in the complex plane. For the adiabatic problem we therefore find, that

$$\boldsymbol{X}_k(t) = \hat{R}_{\omega_k t}\boldsymbol{X}_k(t=0). \tag{109}$$

For the numerical experiments presented in Sect. 6 we use the first non-trivial eigenmode for initialization corresponding to the non-zero eigenvalue with the smallest magnitude.

F Numerical scheme for asymptotic equations

By providing a closure $(Q_0, \boldsymbol{Q}_1) = F(\boldsymbol{X}, u_\theta, t)$ Eqs. (3) and (1) form a closed set of partial differential equations which in general cannot be solved analytically. Thus, we further analyze the structure of these equations seeking for an adapted numerical method to allow for efficient and stable time integration.

Weber [45] first presented a numerical scheme for solving the coupled system (3) and (1). While the author followed a method-of-lines approach discretizing the spatial derivatives by fourth-order approximations to solve the resulting system of ordinary differential equations by generic integrators, it turned out that for certain settings it becomes stiff, and we therefore try to take advantage of the equations' structure revealed in Appendix 7 to allow for a more efficient time integration by using adapted methods. We revisited all the equations presented by Päschke et al. [26] needed for closure and further performed the split of (3) into linear and non-linear contributions which lead to a quasi-Hamiltonian substructure giving rise to the numerical scheme to be presented Sect. 7. In addition to the centerline equation (107) time evolution of the tangential velocity is re-written as

$$\partial_t u_\theta + u_{r,00}\partial_r u_\theta + w_0 \partial_z u_\theta = -\left(u_{r,*} + u_{r,00}\right)\left(\frac{u_\theta}{r} + f\right) \tag{110}$$

to identify an advection term (in polar coordinates) on the left-hand side and source terms on the right-hand side. The integration scheme of this equation is presented in Sect. 7.

By our analysis we learned that the system of equations (107) and (110) is assembled by prototypes of partial differential equations that are (1) advection equation, (2) Schrödinger equation, and (3) non-linearly coupled ordinary differential equations (source terms).

Aiming at the scope of this work we restrict to asymmetric diabatic heating which allows to drop all terms referring to symmetric vertical and radial motions. We further neglect background wind shear. Hence, we drop all the advective terms from Eqs. (107) and (110) and set $u_s = 0$.

F.1 Integration of centerline

For the integration of the centerline position the general solution strategy is to integrate nonlinear source terms by the trapezoidal rule and the Sturm–Liouville operator (after appropriate spatial discretization) by the implicit midpoint rule. The choice of the latter is based on the principle of preserving unitarity during integration of the linear part of the equation. We also dropped contributions according to shear as they are not discussed in Sect. 6. The composition of the sub-steps reads:

$$X^* = \frac{1}{2}\Delta t\, Q(u^n, X^n, t^n) + X^n \tag{111a}$$

$$X^{**} = \left(\mathbb{1} - \frac{1}{2} i\,\Delta t\,\hat{H}\left(u^{n+1/2}\right)\right) X^* \tag{111b}$$

$$X^{n+1} = \left(\mathbb{1} + \frac{1}{2} i\,\Delta t\,\hat{H}\left(u^{n+1/2}\right)\right)^{-1} \left(\frac{1}{2}\Delta t\, Q(u^{n+1}, X^{n+1}, t^{n+1}) + X^{**}\right) \tag{111c}$$

$\mathbb{1}$ represents the identity operator. For the evaluation of $\hat{H}$ we need $u^{n+1/2}$ which we obtain by the first-order predictor $u^{n+1/2} = u^*$. To maintain stability the timestep is completed by implicitly solving for X^{n+1} taking also u^{n+1} into account which is solved in the subsequent subsection.

F.2 Integration of tangential velocity

After canceling the advection part of Eq. (110), as $u_{r,00}$ and w_0 vanish, only the right-hand side source term proportional to $u_{r,*}$ remains which is treated numerically by applying the trapezoidal rule. The integration scheme for one timestep of size Δt reads

$$u^* = -\frac{1}{2}\Delta t\, u^n_{r,*}\left(\frac{u^n}{r} + f\right) + u^n\,, \tag{112a}$$

$$u^{n+1} = -\frac{1}{2}\Delta t u_{r,*}^{n+1}\left(\frac{u^{n+1}}{r} + f\right) + u^*\,, \tag{112b}$$

For brevity we dropped the $_\theta$ sub-index. Same as for Eq. (111c), it becomes obvious that the final step of the integration involves an implicit solution strategy as the term $u_{r,*}^{n+1}$ depends on both X and u at time level $n+1$.

F.3 Coupled integration

In both, explicit and implicit forcing, the equations are couples to each other. The latter requires information of X and u at time t^{n+1}. A common procedure (c.f. [1,42]) solving problems of this kind is to formulate it as a non-linear fixed-point problem and lagging X^{n+1} and u^{n+1} one iteration behind when evaluating Q and $u_{r,*}$:

$$X^{n+1,0} = X^{**} \tag{113a}$$

$$u^{n+1,0} = u^* \tag{113b}$$

$$X^{n+1,\nu} = \left(\mathbb{1} + \frac{1}{2} i\Delta t\hat{H}\left(u^{n+1/2}\right)\right)^{-1}\left(\frac{1}{2}\Delta t Q(u^{n+1,\nu-1}, X^{n+1,\nu-1}, t^{n+1}) + X^{**}\right) \tag{113c}$$

$$u^{n+1,\nu} = -\frac{1}{2}\Delta t u_{r,*}^{n+1,\nu-1}\left(\frac{u^{n+1,\nu}}{r} + f\right) + u^* \tag{113d}$$

F.4 Details on the spatial discretization

The equations are discretized on an equidistant grid allowing for straightforward finite-difference approximations of the derivate operators. Boundary conditions are accommodated by extending the grid covering the physical domain plus a ghost layer of two cells. Solution values are stored in cell-centers while first derivate are computed typically on the corresponding faces.

Prototypical differential expressions such as $\alpha\partial_z(\beta\partial_z\psi)$ are discretized as:

$$\alpha\partial_z(\beta\partial_z\psi)|_{z=z_i} = \frac{1}{\Delta z^2}\alpha_i\left(\beta_{i+1/2}\left(\psi_{i+1}-\psi_i\right) - \beta_{i-1/2}\left(\psi_i - \psi_{i-1}\right)\right) \tag{114}$$

Integrals are computed via the trapezoidal rule where ghost cells are obtained by quadratic extrapolation. We further include an option to apply hyper-viscosity to the centerline stabilizing time integration for activated diabatic heating. Further details may be taken from the source code available on demand by the corresponding author.

G Details on the numerical implementation

G.1 Dimensional variables

Though the derivation outlined above is carried out in terms of non-dimensional variables, for the actual implementation into EULAG we used dimensional quantities of which some details will be presented in this section. In the spirit of asymptotic analysis, for reconstructing dimensional variables and to formulate leading-order relations we use leading-order or next-to-leading-order modes. The following formulas are expressed for non-vanishing Coriolis parameters in the gradient wind regime. However, they are also valid in the cyclostrophic regime by setting $f_{\mathrm{ref}} = 0$.

Before presenting specific relation which arise from the asymptotic analysis, we want to relate the expansion modes with mean background values, denoted by bars $\overline{(\cdot)}$ and perturbations, denoted by primes $(\cdot)'$.

$$\overline{\rho} = \rho_{\mathrm{ref}}\left(\rho_0 + \delta^2\rho_2 + \delta^4\hat{\rho}_4 + \mathscr{O}\left(\delta^5\right)\right) \qquad \rho' = \rho_{\mathrm{ref}}\left(\delta^4\hat{\rho}^{(4)} + \mathscr{O}\left(\delta^5\right)\right) \tag{115a}$$

$$\overline{p} = p_{\mathrm{ref}}\left(p_0 + \delta^2 p_2 + \delta^4\hat{p}_4 + \mathscr{O}\left(\delta^5\right)\right) \qquad p' = p_{\mathrm{ref}}\left(\delta^4\hat{p}^{(4)} + \mathscr{O}\left(\delta^5\right)\right) \tag{115b}$$

$$\overline{\Theta} = T_{\mathrm{ref}}\left(\Theta_0 + \delta^2\Theta_2 + \delta^4\hat{\Theta}_4 + \mathscr{O}\left(\delta^5\right)\right) \qquad \Theta' = T_{\mathrm{ref}}\left(\delta^4\hat{\Theta}^{(4)} + \mathscr{O}\left(\delta^5\right)\right) \tag{115c}$$

Furthermore, we have

$$u_\theta = \boldsymbol{u} \cdot \boldsymbol{e}_\theta = u_{\mathrm{ref}} \left(\frac{1}{\delta} u_\theta^{(0)} + \mathscr{O}(1) \right) \tag{116a}$$

$$w = u_{\mathrm{ref}} \left(\delta \hat{w}^{(1)} + \mathscr{O}\left(\delta^2\right) \right) \tag{116b}$$

G.1.1 Pressure

Equation (27a) balances pressure gradient with radial forces. We find the dimensional version as

$$\frac{1}{\rho} \frac{\partial p}{\partial r} = \frac{u_\theta^2}{r} + f_{\mathrm{ref}} u_\theta \,. \tag{117}$$

G.1.2 Potential temperature

For the deviation of potential temperature from its background mean value $\overline{\Theta}$ we have for the first Fourier modes

$$\boldsymbol{\Theta}_1' = -\frac{\overline{\Theta}}{g} \frac{1}{\overline{\rho}} \frac{\partial p}{\partial r} \frac{\partial \boldsymbol{X}}{\partial z} \,. \tag{118}$$

G.1.3 Vertical velocity

In general, i.e., for arbitrary heating, the vertical velocity takes the following form in physical dimensions:

$$w = \frac{1}{\frac{\mathrm{d}\Theta}{\mathrm{d}z}} \left(Q_\Theta + \frac{\overline{\Theta}}{g} \frac{u_\theta}{r} \left(\frac{u_\theta^2}{r} + u_\theta f_{\mathrm{ref}} \right) \left(\hat{R}_{-\pi/2} \frac{\partial \boldsymbol{X}}{\partial z} \right) \cdot \boldsymbol{e}_r \right) \tag{119}$$

G.1.4 Diabatic heating

Finally, we defined a heating dipole aligned with an angle θ_0 relative to the tilt direction:

$$Q_\Theta^{\theta_0} = \frac{\overline{\Theta}}{g} \frac{u_\theta}{r} \left(\frac{u_\theta^2}{r} + u_\theta f_{\mathrm{ref}} \right) \left(\hat{R}_{\theta_0} \frac{\partial \boldsymbol{X}}{\partial z} \right) \cdot \boldsymbol{e}_r \tag{120}$$

G.2 Convergence results

In addition to comparing both, simulation results of three-dimensional and asymptotic equations, we check for convergence of each numerical schemes. For both simulations we check for self-consistency by comparing results at increasing resolution with high-resolved reference. Convergence of the EULAG simulations is displayed in Fig. 20 showing second-order convergence.
The numerical scheme solving the asymptotic equation on the other hand is tested by evolving

$$\boldsymbol{X}(t = 0) = (\cos(z\pi / z_{\max}), 0)^{\mathrm{T}} \tag{121}$$

for $T = 0.1$ (in asymptotic units) and comparing solutions of different resolutions against a reference solution with 1280 grid points. The results are plotted in Fig. 21 indicating second-order convergence as expected.

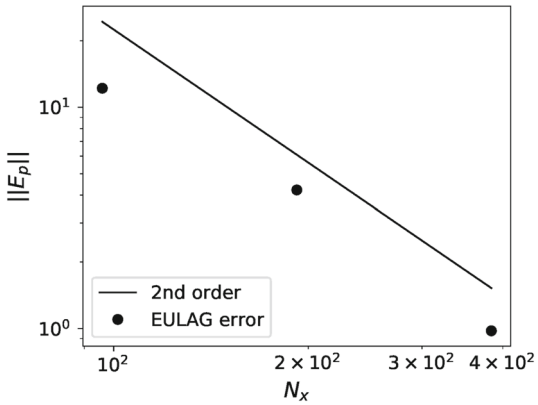

Fig. 20 Error convergence for EULAG simulations. The maximum deviation of perturbation pressure from a reference solution with $768 \times 768 \times 384$ grid points at $t = 1$ day is plotted (solid line for reference)

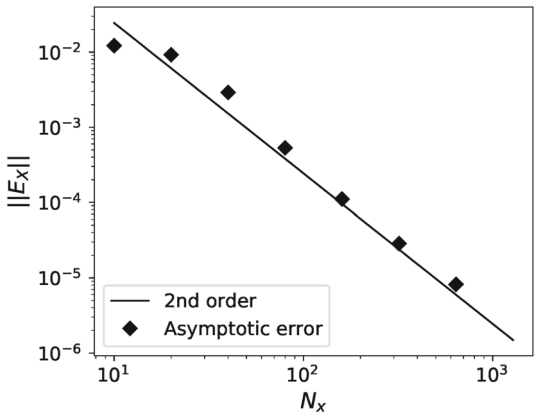

Fig. 21 Convergence plot for numerical scheme solving the asymptotic equations. Error values indicated by diamond markers are computed as the difference between the current solution a reference solution with 1280 grid points

H Anti-stagnation test

In sec. 6.2, we presented and discussed the results of an *adiabatic* reference as well as tests showing the results of asymmetric diabatic heat release under different angles θ_0 between tilt and heating dipole. We named these experiments *stagnation test* ($\theta_0 = \pi/2$), *intensification test* ($\theta_0 = \pi$) and *attenuation test* ($\theta_0 = 0$). Here we present the *anti-stagnation test* with $\theta_0 = -\pi/2$ resulting in a heating dipole that is positively correlated with

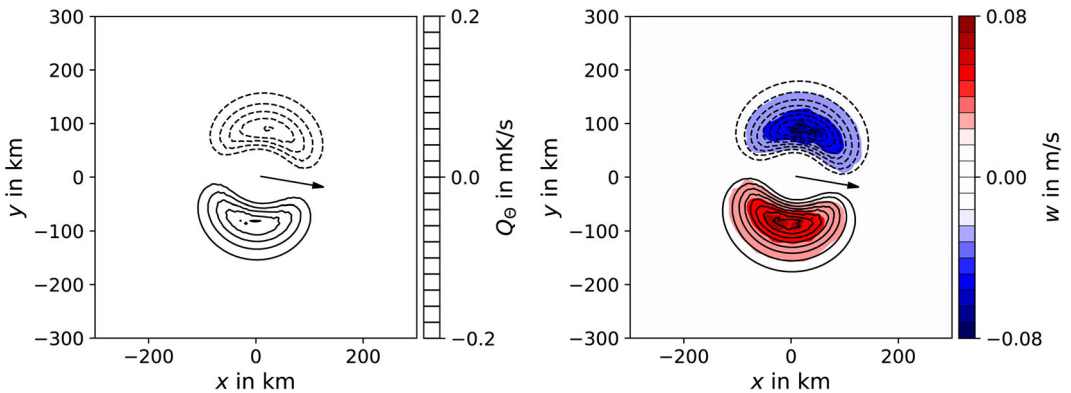

Fig. 22 Diabatic heating and resulting vertical velocity on *anti-stagnation test* (cmp. with Fig. 8) (color figure online)

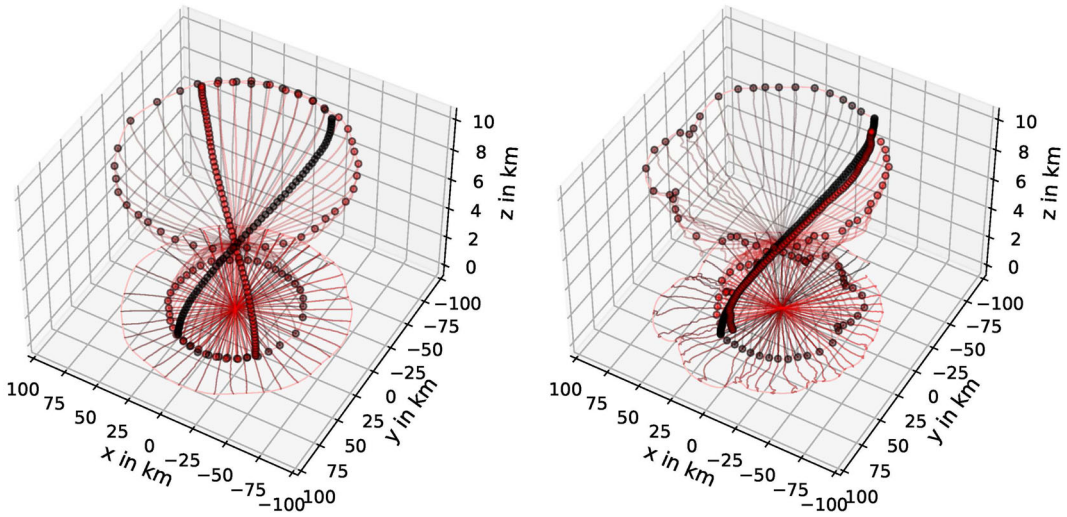

Fig. 23 Centerline evolution of anti-stagnation test (cmp. with Fig. 10)

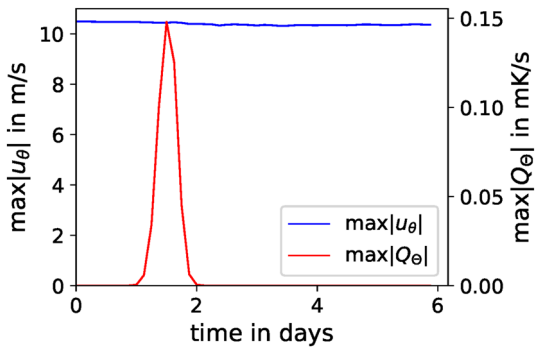

Fig. 24 Time series of maximum tangential velocity of anti-stagnation test (cmp. with Fig. 9) (color figure online)

the tilt-induced adiabatic vertical velocity dipole. In analogy to Figs. 8, 10, and 9, we present vertical velocity, centerline time evolution and the time series of maximum tangential velocity in Figs. 22, 23, and 24.

During the phase of active heating, the vertical velocity essentially doubles in amplitude (cf. Fig. 7) and the centerline precession frequency is enhanced (cf. Fig. 6). The maximum of tangential velocity, however, remains approximately constant. We obtained the same result from the stagnation test since, as here, the heating dipole is orthogonal to the tilt vector yielding $u_{r,*} = 0$ and therefore no tendency in the tangential velocity.

References

1. Benacchio, T., Klein, R.: A semi-implicit compressible model for atmospheric flows with seamless access to soundproof and hydrostatic dynamics. Mon Weather Rev **147**(11), 4221–4240 (2019). https://doi.org/10.1175/MWR-D-19-0073.1
2. Callaghan, J.: Asymmetric inner core convection leading to tropical cyclone intensification. Trop. Cyclone Res. Rev. **6**, 55–66 (2017)
3. Chen, H., Gopalakrishnan, S.G.: A study on the asymmetric rapid intensification of hurricane earl (2010) using the hwrf system. J. Atmos. Sci. **72**(2), 531–550 (2015). https://doi.org/10.1175/JAS-D-14-0097.1
4. Davis, C.A., Jones, S.C., Riemer, M.: Hurricane vortex dynamics during Atlantic extratropical transition. J. Atmos. Sci. **65**(3), 714–736 (2008). https://doi.org/10.1175/2007JAS2488.1
5. Dunkerton, T.J., Montgomery, M.T., Wang, Z.: Tropical cyclogenesis in a tropical wave critical layer: easterly waves. Atmos. Chem. Phys. **9**, 5587–5646 (2009)
6. Emanuel, K.A.: An air-sea interaction theory for tropical cyclones. Part I: steady-state maintenance. J. Atmos. Sci. **43**(6), 585–605 (1986). https://doi.org/10.1175/1520-0469
7. Emanuel, K.A.: Tropical cyclones. Annu. Rev. Earth Planet. Sci. **31**, 75–104 (2003)
8. Hazelton, A.T., Hart, R.E., Rogers, R.F.: Analyzing simulated convective bursts in two Atlantic hurricanes. part ii: Intensity change due to bursts. Mon. Weather Rev. **145**(8), 3095–3117 (2017a). https://doi.org/10.1175/MWR-D-16-0268.1

9. Hazelton, A.T., Rogers, R.F., Hart, R.E.: Analyzing simulated convective bursts in two Atlantic hurricanes. Part i: burst formation and development. Mon. Weather Rev. **145**(8), 3073–3094 (2017b). https://doi.org/10.1175/MWR-D-16-0267.1
10. Jones, S.: The evolution of vortices in vertical shear i: initially barotropic vortices. Q. J. R. Meteorol. Soc. **121**, 821–851 (1995)
11. Klein, R.: Scale-dependent asymptotic models for atmospheric flows. Ann. Rev. Fluid Mech. **42**, 249–274 (2010)
12. Kuhn, W.R., London, J.: Infrared radiative cooling in the middle atmosphere (30–110 km). J. Atmos. Sci. **26**(2), 189–204 (1969). https://doi.org/10.1175/1520-0469
13. Leighton, H., Gopalakrishnan, S., Zhang, J.A., Rogers, R.F., Zhang, Z., Tallapragada, V.: Azimuthal distribution of deep convection, environmental factors, and tropical cyclone rapid intensification: a perspective from hwrf ensemble forecasts of Hurricane Edouard (2014). J. Atmos. Sci. **75**(1), 275–295 (2018). https://doi.org/10.1175/JAS-D-17-0171.1
14. Lorenz, E.N.: Generation of available potential energy and the intensity of the general circulation. Technical report, UCLA (1955)
15. Lorenz, E.N.: The nature and theory of the general circulation of the atmosphere, parts i-iii. TP115 218, World Meteorological Organization (1967)
16. Marks, F.D.: Hurricanes. In: Handbook of Weather, Climate, and Water: Dynamics, Climate, Physical Meteorology, Weather Systems, and Measurements. Wiley, New York (2003)
17. Marks, F.D., Houze, R.A., Jr., Gamache, J.F.: Dual-aircraft investigation of the inner core of hurricane norbert. Part I: kinematic structure. J. Atmos. Sci. **49(11), 919–942**, 06 (1992). https://doi.org/10.1175/1520-0469
18. Menelaou, K., Yau, M.K.: On the role of asymmetric convective bursts to the problem of hurricane intensification: radiation of vortex rossby waves and wave-mean flow interactions. J. Atmos. Sci. **71**(6), 2057–2077 (2014). https://doi.org/10.1175/JAS-D-13-0343.1
19. Montgomery, M., Smith, R.: On the applicability of linear, axisymmetric dynamics in intensifying and mature tropical cyclones. Fluids **2**(4), 69 (2017). https://doi.org/10.3390/fluids2040069
20. Smith, R.K., Montgomery, M.T.: Recent developments in the fluid dynamics of tropical cyclones. Ann. Rev. Fluid Mech. **49**, 1–32 (2017)
21. Nguyen, L.T., Molinari, J., Thomas, D.: Evaluation of tropical cyclone center identification methods in numerical models. Mon. Weather Rev. **142**(11), 4326–4339 (2014). https://doi.org/10.1175/MWR-D-14-00044.1
22. Nolan, D.S., Grasso, L.D.: Nonhydrostatic, three-dimensional perturbations to balanced, hurricane-like vortices. Part ii: symmetric response and nonlinear simulations. J. Atmos. Sci. **60**(22), 2717–2745 (2003)
23. Nolan, D.S., Montgomery, M.T.: Nonhydrostatic, three-dimensional perturbations to balanced, hurricane-like vortices. Part i: linearized formulation, stability, and evolution. J. Atmos. Sci. **59**(21), 2989–3020 (2002)
24. Nolan, D.S., Moon, Y., Stern, D.P.: Tropical cyclone intensification from asymmetric convection: energetics and efficiency. J. Atmos. Sci. **64**, 3377–3405 (2007)
25. Papke, A.: Atmospheric Vortex Stability Under Vertical Shear. Freie Universität, Berlin (2017). (**PhD thesis**)
26. Päschke, E., Marschalik, P., Owinoh, A., Klein, R.: Motion and structure of atmospheric mesoscale baroclinic vortices: dry air and weak environmental shear. J. Fluid Mech. **701**, 137–170 (2012)
27. Pauluis, O.M., Zhang, F.: Reconstruction of thermodynamic cycles in a high-resolution simulation of a hurricane. J. Atmos. Sci. **74**(10), 3367–3381 (2017). https://doi.org/10.1175/JAS-D-16-0353.1
28. Polvani, L.M.: Two-layer geostrophic vortex dynamics. Part 2. Alignment and two-layer V-states. J. Fluid Mech. **225**, 241–270 (1991). https://doi.org/10.1017/S0022112091002045
29. Prusa, J., Smolarkiewicz, P., Wyszogrodzki, A.: EULAG, a computational model for multiscale flows. Comput. Fluids **37**, 1193–1207 (2008). https://doi.org/10.1016/j.compfluid.2007.12.001
30. Reasor, P.D., Montgomery, M.T.: Three-dimensional alignment and corotation of Weak, tc-like vortices via linear vortex Rossby waves. J. Atmos. Sci. **58**, 2306–2330 (2001)
31. Reasor, P.D., Montgomery, M.T.: Evaluation of a heuristic model for tropical cyclone resilience. J. Atmos. Sci. **72**, 1765–1782 (2015)
32. Reasor, P.D., Montgomery, M.T., Marks, F.D., Jr., Gamache, J.F.: Low-wavenumber structure and evolution of the hurricane inner core observed by airborne dual-Doppler radar. Mon. Weather Rev. **128**, 1653–1680 (2000)
33. Reasor, P.D., Montgomery, M.T., Grasso, L.D.: A new look an the problem of tropical cyclones in vertical shear flow. J. Atmos. Sci. **61**(1), 3–22 (2004)
34. Rios-Berrios, R.: Impacts of radiation and cold pools on the intensity and vortex tilt of weak tropical cyclones interacting with vertical wind shear. J. Atmos. Sci. **77**, 669–689 (2020)
35. Rivoire, L., Birner, T., Knaff, J.A., Tourville, N.: Quantifying the radiative impact of clouds on tropopause layer cooling in tropical cyclones. J. Clim. **33**, 6361–6376 (2020)
36. Rogers, R.F., Reasor, P.D., Zhang, J.F.: Multiscale structure and evolution of hurricane Earl (2010) during rapid intensification. Mon. Weather Rev. **143**, 536–562 (2015)
37. Rotunno, R., Emanuel, K.A.: An air-sea interaction theory for tropical cyclones. Part II: evolutionary study using a nonhydrostatic axisymmetric numerical model. J. Atmos. Sci. **44**(3), 542–561 (1987). https://doi.org/10.1175/1520-0469
38. Ruppert, J.H., O'Neill, M.E.: Diurnal cloud and circulation changes in simulated tropical cyclones. Geophys. Res. Lett. **46**, 502–511 (2019)
39. Ryglicki, D.R., Cossuth, J.H., Hodyss, D., Doyle, J.: The unexpected rapid intensification of tropical cyclones in moderate vertical wind shear. Part I: overview and observations. Mon. Weather Rev. **146**(11), 3773–3800 (2018). https://doi.org/10.1175/MWR-D-18-0020.1
40. Schecter, D.A.: Response of a simulated hurricane to misalignment forcing compared to the predictions of a simple theory. J. Atmos. Sci. **72**(3), 1235–1260 (2015). https://doi.org/10.1175/JAS-D-14-0149.1
41. Smith, R.K., Zhang, J.A., Montgomery, M.T.: The dynamics of intensification in a hurricane weather research and forecasting simulation of hurricane earl (2010). Q. J. R. Meteorol. Soc. **143**(702), 293–308 (2017). https://doi.org/10.1002/qj.2922

42. Smolarkiewicz, P.K., Kühnlein, C., Wedi, N.P.: A consistent framework for discrete integrations of soundproof and compressible PDEs of atmospheric dynamics. J. Comput. Phys. **263**, 185–205 (2014). https://doi.org/10.1016/j.jcp.2014.01.031
43. Teschl, G.: Ordinary Differential Equations and Dynamical Systems, volume 140 of Graduate Studies in Mathematics. American Mathematical Society, Providence (2012)
44. Wang, Y., Holland, G.J.: Tropical cyclone motion and evolution in vertical shear. J. Atmos. Sci. **53**(22), 3313–3332 (1996)
45. Weber, T.: Analyse und numerische Berechnung atmosphärischer Wirbel im Regime tropischer Stürme. Freie Universität Berlin, FB für Mathematik und Informatik, Master's thesis, Berlin (2011)